Protrusion force and cell-cell adhesion play a critical role in collective tumor cluster migration

Huijing Wang[1,†,*],
Catalina Ardila[2,*],
Ajita Jindal[2],
Vaishali Aggarwal[2],
Weikang Wang[#,§],
Jonathan Vande Geest[3,4],
Yi Jiang[5],
Jianhua Xing[1,6,¶],
Shilpa Sant[2,3,4,7,$,¶]

[*]Co-first with equal contribution.
[¶]Corresponding authors

Research was conducted at the following address:

[1]Department of Computational & Systems Biology, School of Medicine, University of Pittsburgh, Pittsburgh, PA, USA

[2]Department of Pharmaceutical Sciences, School of Pharmacy, University of Pittsburgh, Pittsburgh, PA, USA

[3]Department of Bioengineering, Swanson School of Engineering, University of Pittsburgh, Pittsburgh, PA, USA

[4]McGowan Institute for Regenerative Medicine, University of Pittsburgh, Pittsburgh, PA, USA

[5]Department of Mathematics and Statistics, Georgia State University, Atlanta, GA, USA

[6]Department of Physics and Astronomy, University of Pittsburgh, Pittsburgh, PA, USA

[7]UPMC-Hillman Cancer Center, University of Pittsburgh, Pittsburgh, PA, USA

Present address:

[†]Department of Physics, Carnegie Mellon University, Pittsburgh, PA, USA

[#]CAS Key Laboratory for Theoretical Physics, Institute of Theoretical Physics, Chinese Academy of Sciences, Beijing, China

[§]School of Physical Sciences, University of Chinese Academy of Sciences, Beijing, China

[$]Department of Pharmaceutical Sciences, College of Pharmacy, University of Illinois Chicago, Chicago, IL, USA

Conflict of Interest Statement: The authors declare no potential conflicts of interest.

Abstract

While collective migration is shown to enhance invasive and metastatic potential in cancer, the mechanisms driving this behavior and regulating tumor migration plasticity remain poorly understood. This study provides a mechanistic framework explaining the emergence of different modes of collective migration under hypoxia-induced secretome. We focus on the interplay between cellular protrusion force and cell-cell adhesion using collectively migrating three-dimensional microtumors as models with well-defined microenvironment. Large microtumors show directional migration due to intrinsic hypoxia, while small microtumors exhibit radial migration in response to hypoxic secretome. Here, we developed the minimal **m**ulti-**s**cale **m**icrotumor **m**odel (MSMM) to elucidate underlying mechanisms. We identified distinct migration modes within specific regions of protrusion force and cell-cell adhesion parameter space. We show that sufficient cellular protrusion force is crucial for both, radial and directional collective microtumor migration. Radial migration emerges when sufficient cellular protrusion force is generated, driving neighboring cells to move collectively in diverse directions. Within migrating tumors, strong cell-cell adhesion enhances the alignment of cell polarity, breaking the symmetric angular distribution of protrusion forces, and leading to directional microtumor migration. The integrated results from the experimental and computational models provide fundamental insights into collective migration in response to different microenvironment stimuli.

Introduction

Cancer metastasis is a multi-step process that involves migration, invasion and dissemination of tumor cells from the primary tumor site to the distant organs to establish secondary metastases [1]. There is growing evidence that cancer metastases and invasion are driven by the movement of small tumor cell clusters rather than individual cells [2]. This phenomenon is called collective migration, which refers to the coordinated movement of cells as a single unit due to the presence of strong cell-cell adhesion forces maintained by cell-cell junctions [3-6]. The role of collective cell migration in cancer metastasis was first reported in the 1950s in a study that showed presence of both individual cells as well as collective tumor clusters in a cancer patient's blood. The researchers established that these circulating tumor cell (CTCs) clusters originate from solid tumors and are shed into the bloodstream [7, 8]. It is also reported that the tumor clusters move more efficiently through the bloodstream when disseminated as a group of cells [2], and are capable of retaining their epithelial cell adhesion machinery that contributes greatly to metastatic progression [9]. Although collective migration is known to drive several other biological processes such as wound healing and embryogenesis, the underlying mechanisms behind various modes of collective migration are poorly explored. Symmetry breaking is an essential process underlying cellular fate decision, such as polarization, migration, and division. For example, a local asymmetric distribution of Ras-GTP signal triggers cytoskeletal rearrangement, thus establishing single cell polarity in eukaryotic amoeboid cells for migration [10-12]. However, the mechanistic interactions for spontaneous symmetry breaking in collective migration of microtumors has not been fully elucidated [11, 13]. Unraveling these mechanisms can lead to the discovery of key biomarkers and therapeutic targets to limit or even prevent collective migration and invasion of cancer cells to other organs.

A major hurdle in studying collective migration in tumor clusters is the lack of suitable physiologically relevant three-dimensional (3D) *in vitro* models that can recapitulate collective

cluster migration. 2D *in vitro* assays such as Boyden chamber assays or the scratch assay [14, 15] have been widely used to study single cell migration and invasion; however, this technique is not suitable for studying collective cluster migration [16], because these 2D assays cannot quantify collective tumor migration, the tumor shape, or cell-cell interactions [17]. To unravel the influence of a hypoxic tumor microenvironment on the emergence of migratory phenotype, we have previously developed a hydrogel device with microwell arrays to generate uniform-sized large (600 µm) and small (150 µm) microtumors from the same non-invasive parental T47D breast cancer cells [18-25]. We have shown that the large microtumors develop hypoxic signatures as early as day 1 and exhibit collective migration [19], where whole tumor clusters migrate out of the hydrogel microwell. On the other hand, the non-hypoxic small microtumors do not migrate over the culture period. However, when treated with the secretome from large hypoxic microtumors, the non-migratory small microtumors exhibit starburst-like radial migration [21]. Thus, microtumors made of the same parental T47D cells exhibit plasticity in collective migration where the directional and radial modes of collective migration emerged in response to two different microenvironmental stimuli, tumor-intrinsic hypoxia, and hypoxic secretome, respectively. In this work, we set out to investigate the plausible mechanisms underlying emergence of these distinct migratory phenotypes by using pharmacological perturbations and mathematical approaches.

Tumor migration is a result of a series of biological processes [26] and is often associated with mechanical cues in the microenvironment due to shear stresses, cell-cell and cell-ECM interactions [27], where tumor cells respond to signaling pathways such as Rho GTPases by polarizing and extending actin polymerization-driven cell membrane protrusions towards the extracellular cues, such as growth factors or chemokines [28-30]. Tumor cell plasticity or increased metabolism among others have been proposed as potential mechanisms for tumor migration including single cell migration, collective cell migration, and cohort/cluster migration [31]. However, there is no consensus on how different migratory phenotypes emerge. In this work, we

investigated interplay between protrusion force and cell-cell adhesion to explain the plasticity of collective tumor migration in response to different microenvironmental stimuli. To elucidate potential mechanisms underlying emergence of different tumor migration modes such as directional cluster migration and radial migration, we designed a tumor migration model using the **m**ulti-**s**cale **m**icrotumor **m**odel (MSMM) framework, based on *in vitro* observations in our 3D microtumor experiments. Our model incorporates cellular mechanics, such as cell shape distortion, force-driven motility, and cell-cell adhesion. By fine-tuning the protrusion and cell-cell adhesion forces in our MSMM, we can recapitulate both the directional and the radial migration modes observed experimentally in response to different stimuli. Combining pharmacological perturbations and mathematical approaches, we demonstrate that threshold protrusion force is necessary for collective migration, and distinct migration modes emerge due to competition between protrusion forces and cell-cell adhesion forces.

Results

1. Tumor-intrinsic hypoxia induces directional migration in large microtumors while hypoxic secretome induces radial migration in small microtumors.

We have previously fabricated hydrogel microwell arrays (**Figure 1a**) for studying microtumor migration under controlled microenvironments [18, 23]. The uniform-sized microtumors are generated from the same non-invasive parental T47D breast cancer cells using microwells either with a diameter of 600 µm (denoted as large 600 microtumors) or with a diameter of 150 µm (denoted as 150 microtumors). Our prior studies indicated that the large 600D6 microtumors displayed migratory behavior whereas the small 150D6 microtumors remained non-migratory for the entire culture time of six days (where D6 indicates six days of culture time) [19-21, 23]. Large 600 microtumors spontaneously developed tumor-intrinsic hypoxia as early as day 1, started directional collective movement of the whole tumor cluster from day 3, and upregulated expression of mesenchymal markers without loss of E-cadherin [19, 21, 23]. This directional

collective migration is characterized by an initial movement of the tumor towards one side of the microwell and eventually “migrating out” of the microwell (**Figure 1b)** [19, 20, 23]. We further treated the non-migratory non-hypoxic small 150 microtumors with conditioned medium (CM, hypoxic secretome) of the migratory large microtumors starting from day 3 (denoted as 150CM microtumors). The secretome treatment induced a distinct migratory phenotype in 150CM microtumors, where the cells migrated outward radially from the center of the microtumor (**Figure 1c**). The secretome-induced radial migration is characterized by the appearance of multiple migratory fronts in random directions.

To understand the biophysical mechanisms for the emergence of such distinct tumor migration modes, we performed RNA microarray analysis for directionally migrating 600D6 tumors and radially migrating 150CM tumors, using non-migratory 150D6 as a reference [23]. We focused on the differentially expressed genes, which were further enriched for Gene Ontology (GO) terms for biological processes (BP). GO terms describing biophysical processes during tumor migration include “Actin filament organization”, “Biological adhesion”, “Regulation of cytoskeleton organization” and so on (**Figure 1d**). Microarray analysis of hypoxia-induced directional migration (600D6) revealed that cell adhesion-related terms such as “Cell-cell adhesion”, “Biological adhesion” and “Positive regulation of locomotion” were the top positively enriched BP with the highest normalized enrichment scores (NES). The GO term “Biological adhesion” included 131 genes that were differentially expressed in directionally migrating 600D6 compared to non-migratory 150D6. In the analysis of secretome-induced radial migration, *i.e.,* 150CM microtumors, cytoskeletal organization-related terms such as “Positive regulation of cytoskeleton organization”, “Actin filament organization” and “Supramolecular fiber organization” were the top positively enriched BP when compared to non-migratory 150D6 microtumors. Adhesion related processes, such as “Biological adhesion”, “Cell-cell adhesion”, and “Cell junction assembly” were downregulated in 150CM microtumors in contrast to 600D6. On the other hand, protrusion force-

related processes, such as “Actin filament-based process”, “Microtubule polymerization or depolymerization” and “Regulation of cytoskeleton organization” were downregulated in directional migration (600D6) and upregulated in radial migration (150CM). Taken together, GO term enrichment analyses suggest a role of cell adhesion in directional migration phenotype while actin-microtubule cytoskeleton reorganization may be important in secretome-induced radial migration phenotype.

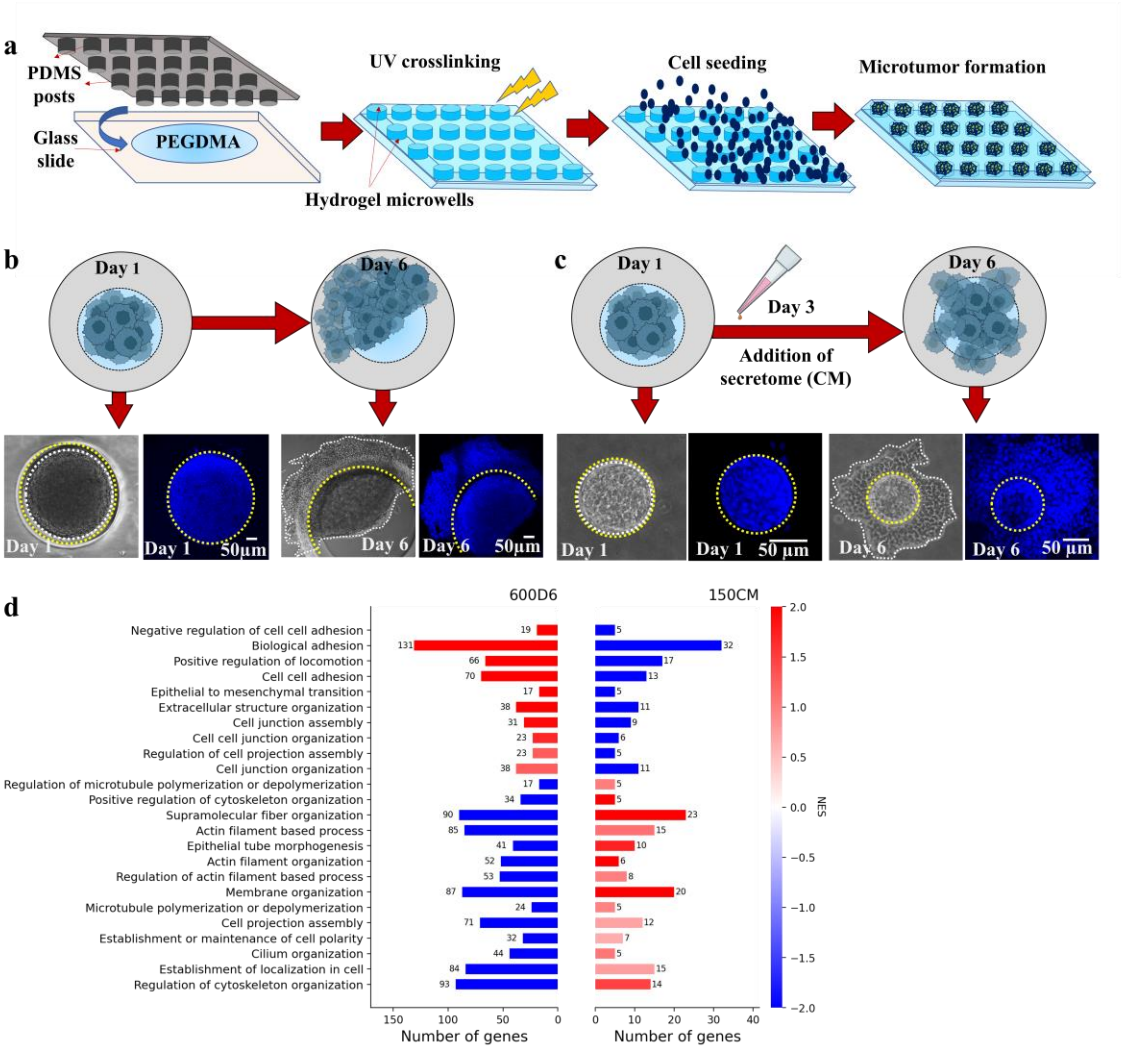

Figure 1. Tumor-intrinsic hypoxia induces directional migration in large microtumors while hypoxic secretome induces radial migration in small microtumors. a. Schematic representation of microfabrication of uniform sized T47D microtumors on hydrogel microarrays. b. Hypoxic 600 μm microtumors exhibit directional migration on day 6. Scale bar: 50 μm c. Treatment of non-migratory 150 μm tumors with hypoxic secretome (CM) gives rise to radial starburst-like migratory phenotype. Scale bar: 50 μm d. Paired gene

set enrichment analysis (GSEA) for GO terms of biological processes related to the biophysical mechanism of microtumor migration, where the left bar plot shows enriched BP for directional migration (600D6) and the right bar plot shows enriched BP for radial migration (150CM). The analysis was done on differentially expressed genes using non-migratory 150D6 as a control group. The normalized enrichment scores (NES) for biological processes are color coded. The names of biological processes are labeled on the y axis. The x axis shows the number of differentially expressed genes for each GO term.

2. A multi-scale microtumor model (MSMM) incorporates intercellular dynamics and intracellular polarity alignment.

Based on the RNA microarray analyses, we propose that differential regulation of the protrusion force and adhesion are plausible mechanisms for the emergence of different tumor migration modes. Protrusion force is generated by localized actin polymerization at the plasma membrane, and cell-cell adhesion is regulated by adherens junction [32]. We hypothesize that the distinct migration behavior in a collectively migrating microtumor emerges from coordination of single-cell migration dynamics, which in turn depends on the strengths of protrusion force within each cell and the adhesion force between the cells. To test our hypothesis, we built a tumor migration model based on the **m**ulti-**s**cale **m**icrotumor **m**odel (MSMM), which is based on the cellular Potts model (CPM) on a 2D plane. The CPM is a lattice-based modeling framework for agent-based modeling, which allows straightforward implementations of various cellular activities, such as motility, adhesion, proliferation, and apoptosis, while keeping realistic cellular shape [33-37]. We first model small 150CM microtumors, where the tumor-intrinsic hypoxia stress is not severe [21, 23]. An illustration of model regime is shown in **Figure 2**.

In the MSMM, cells take up the secretome factors from conditioned media (CM) at a rate depending on their position in the microtumor. For example, cells at the periphery have a higher uptake of secretome than those in the core of the microtumor because less secretome is inside the tumor than at the boundary of the tumor. We simplify the secretome factors as a continuous field that follows a reaction-diffusion dynamics (**Figure 2a**). We assume that the secretome factors up-regulate intracellular protrusion force regulator R, a protein that can promote lamellipodia

formation and mediate protrusion force, leading to increased protrusion force (**Figure 2b**). Potential candidates for the protrusion force regulator may include Rac1, one of the major signaling proteins that regulate cytoskeletal rearrangements [38] and myosin II, a motor protein that controls the force exerted by lamellipodia and filopodia [39]. In MSMM, a cell can protrude in random directions, *i.e.,* cell protrusion attempts can be toward the tumor periphery or tumor center. Intercellular communication through mechanical tension is coupled with the adhesion proteins, which in turn, play an important role in cell-cell adhesion forces. In our model, we describe an "adhesion energy" term, which incorporates intercellular, membrane, and cytoskeletal forces acting on the cell-cell adhesion interface [40] (**Figure 2c**). Each cell can occupy multiple lattice sites, and cell area and perimeter are constrained by energy terms (**Figure 2d-e, Eq S1-3**). Together, the model incorporates intercellular dynamics and intracellular polarity transmission through tension. We implement our model with the open-source software CompuCell3D (CC3D) [37], the details are described in Methods. The model and analysis code can be found in https://github.com/xing-lab-pitt/tumor-migration-model

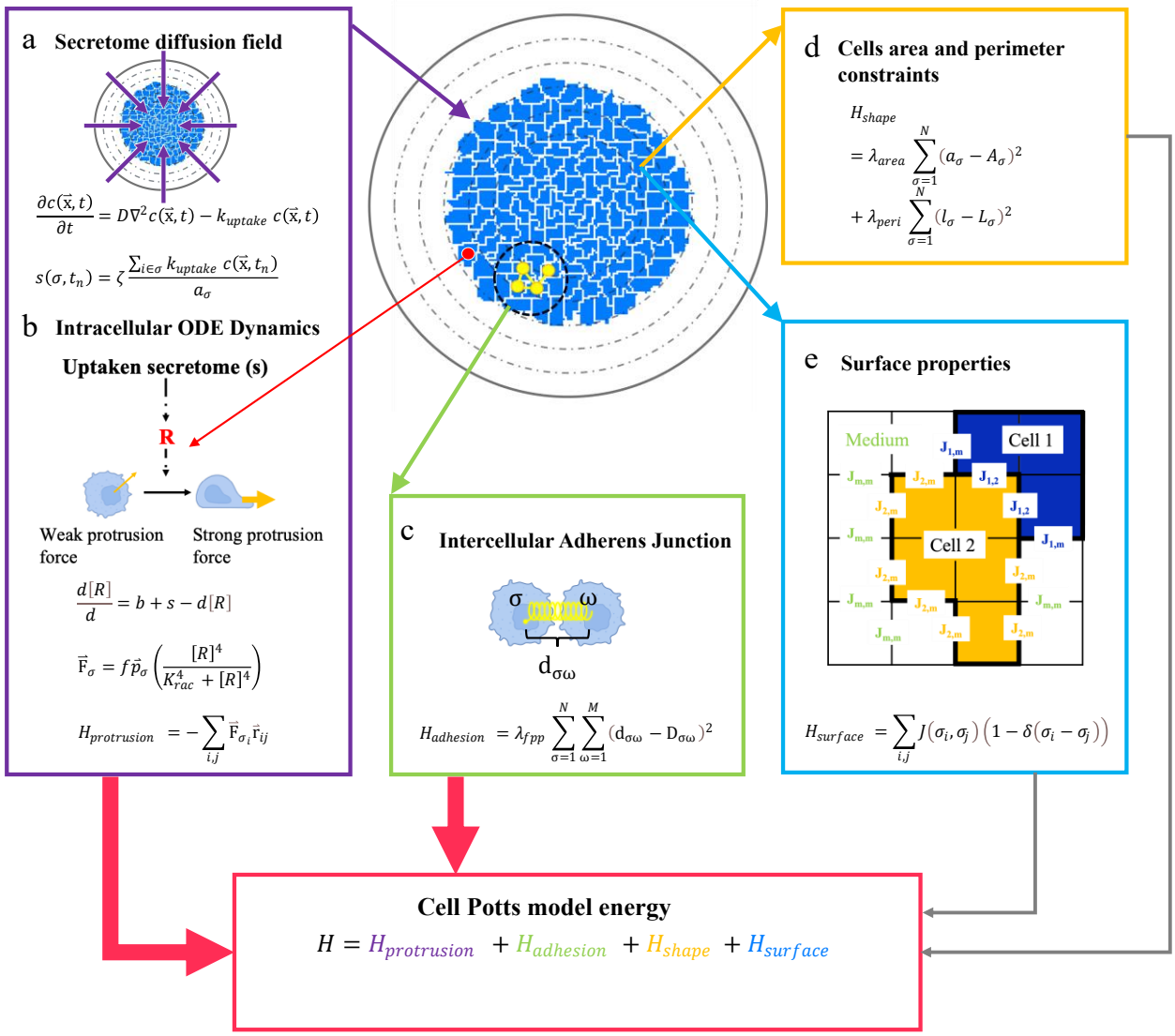

Figure 2. A multi-scale microtumor model (MSMM) scheme consists of four energy terms, including energy from the protrusion force, adhesion energy, shape constraint energy, and surface energy. Tumor cells are colored in blue on the lattice representation, while the secretome signal diffuses into the tumor and is represented as concentric circles. A stochastic multi-scale microtumor model simulation was performed by accepting an energy favorable Monte Carlo move for lattice copy attempts. **a.** At lattice position $\vec{x}$ with a local secretome signal concentration $c(\vec{x},t)$ at time t, a cell (σ) can uptake the secretome signal with an uptake rate constant k_{uptake}. Equation details can be found in Eq. S7-S8. **b.** The averaged secretome signal taken up by each cell (s) induces production of [R] and subsequently generates protrusion force. Details can be found in Eq. S5, S9 and S10. **c.** Cell-cell adhesion is modeled as elastic strings linking the centers of mass for pairs of cells within a defined distance, with a corresponding energy term as a quadratic term for the distance between cells ($d_{\sigma\omega}$) with respect to a target distance ($D_{\sigma\omega}$) (Eq. S4). **d.** For each cell, the cell shape energy H_{shape} is constrained with quadratic energy terms for cell area (a_σ) and perimeter (l_σ), where A_σ and L_σ are the target area and perimeter corresponding to a_σ and l_σ (Eq. S2). **e.** Lattice representation for surface energy $H_{surface}$ between different interfaces, such as cell-cell ($J_{1,2}$), cell-medium ($J_{1,m}$ and $J_{2,m}$) and medium-medium ($J_{m,m}$) (Eq. S3), are shown.

3. The multiscale microtumor model recapitulates distinct migration modes.

To recapitulate the distinct microtumor migration modes induced by tumor-intrinsic hypoxia or secretome [21], we used the multiscale microtumor model to simulate the induction of protrusion force regulator R and cell-cell adhesion in response to the secretome signal (**Figure 3**). Each simulation corresponds to roughly six days of cell culture time to mimic our experimental setup of 3D microtumor migration. Details of the mathematical modeling is in the **supplementary** section, and the parameters used in this model are described in **Tables S1 and S2**.

To better illustrate the interaction between protrusion force and adhesion, we defined an effective force $\hat{F}$ to quantify the real-time protrusion force distribution across cells within a tumor:

$$\hat{F} = f\frac{[R]^4}{K_R^4 + [R]^4}. \tag{1}$$

The impact of $[R]$ on cellular protrusion force is described as a Hill function, with half saturation concentration K_R. Higher $[R]$ can promote stronger protrusion for single cells. Results of our simulation reveal distinct microtumor migration behaviors depending on the model parameters. Specifically, two key parameters that determine tumor migration mode are the maximum protrusion force (f) generated by a cell, and the strength of adhesion interactions between neighboring cells (λ_{fpp}). For example, with $f = 150$ and $\lambda_{fpp} = 20$ (both in arbitrary units), a tumor migrates radially with cells migrating in different directions (**Figure 3a**). With $f = 300$ and $\lambda_{fpp} = 400$, the tumor migrates directionally, where cells collectively migrate as a cluster in one direction. When individual cells migrate radially from the microtumor, the overall convex area of the migrating microtumor increases, while the whole tumor displacement remains low. In contrast, the directionally migrating microtumor display a low convex area and an increase in the whole tumor displacement over time (**Figure 3b**).

To systematically investigate the parameter dependence, we performed a parameter scan over the maximum protrusion force within a range of $[0,300]$ and adhesion strength within a range of $[0,500]$. We characterized the simulated tumors using 19 geometric features (**Supplementary Table S3**, and **Supplementary methods** for details), which cluster the simulated tumors into non-migrating, radially migrating, and directionally migrating tumors (**Figure S1b-c**).

Next, we investigated how the distribution of migration mode changes with values of the maximum protrusion force f and adhesion λ_{fpp} (**Figure 3c**). The radial migration mode is dominant in a region with high protrusion force and low adhesion, while the directional migration mode is dominant in a region with high protrusion force and high adhesion. No migration was observed when the maximum protrusion force f is low ($f < 150$). These results suggest that a certain threshold of protrusion force is necessary for inducing migration. Above this protrusion force threshold, the cell-cell adhesion strength dictates whether tumors assume directional or radial migration mode.

In radially migratory tumors, directions of cell migration are random, while in directional migration, directions of cell migration are more aligned. Such a difference between tumors migrating radially and directionally is also indicated by the different distributions of single cell polarities in these two types of migration modes (**Figure 3d**). Cell polarity ($\vec{p}_\sigma$) is the direction of the force that a cell exerts (**Eq. S11)**. We hypothesize that a stronger cell-cell adhesion leads to a stronger cell polarity correlation between neighboring cells (Eq. S11 and S12). To systematically quantify the correlations between tumor cell polarities during the migration, we defined a normalized average cell polarity ($\vec{p}_\sigma$) in a microtumor as an order parameter [41],

$$\phi = \frac{\left|\sum_{\sigma=1}^{N} \vec{p}_\sigma\right|}{\sum_{\sigma=1}^{N} |\vec{p}_\sigma|}, \tag{2}$$

Where polarity ϕ describes the alignment of migration directions of various cells within the tumor at time t, and it varies between 0 and 1. When $\phi = 0$, the tumor cells move in random directions. When $\phi = 1$, the cell migration directions are completely aligned.

The secretome conditioned medium (CM) activates peripheral cells to generate protrusion forces that drive the tumor into migratory states. As the cell-cell adhesion strength (λ_{fpp}) increases, so does the plateau value of ϕ, indicating that tumors with stronger cell-cell adhesion exhibit higher degree of polarization (**Figure 3e**). To facilitate characterization of the dependence of tumor polarity on cell adhesion strength, we defined a temporally averaged tumor polarity $\bar{\phi}$ as

$$\bar{\phi} = \frac{\sum_{t=1}^{T} \phi}{T}, \tag{3}$$

which describes the alignment of migration directions of all cells within the tumor during the simulation time interval T. It is an order parameter ranging between 0 to 1. When $\bar{\phi} = 0$, the directions of cell migration within a tumor are random, and the tumor likely migrates radially. When $\bar{\phi} = 1$, the directions of migration of all cells within a tumor are aligned, where the tumor likely migrates directionally. Furthermore, we defined the standard deviation of temporally averaged tumor cell polarity P_{STD} as

$$P_{STD} = \sqrt{E\left(\left|\vec{p}_{\sigma,t} - \bar{p}_{\sigma}\right|\right)}, \tag{4}$$

where $\vec{p}_{\sigma,t}$ is the polarity vector for cell σ at time t, and $\bar{p}_{\sigma}$ is the average time series polarity for cell σ. The term P_{STD} describes randomness of the cellular directions of migration over the simulation period in a tumor. Our results suggest that different migration modes show distinct polarity properties (**Figure 3f-h**). In non-migratory tumors, the average polarity $\bar{\phi}$ is low, while the cell migration directions are random, with higher P_{STD} compared to radial and directional migration. Radially migrating tumors are less polarized (low $\bar{\phi}$), with cellular polarity over time (P_{STD}) is less random compared to non-migratory tumors (**Figure 3h**). This leads to multiple migratory fronts in

radial migration where different groups of cells choose to migrate in different directions. Compared to radial migration, directionally migrating tumors have higher average polarity (high $\bar{\phi}$), but similar cell polarity noise over time (low P_{STD}), thus the cells are better aligned in one direction.

In summary, parameter scan simulations reveal that cellular protrusion force and cell-cell adhesion are crucial determinants of distinct migration patterns. First, cells need to exert enough protrusive force to initiate tumor migration. Radial migration manifests when migrating cells align locally and move collectively in diverse directions. Directional migration, on the other hand, results from symmetry breaking. With increased cell-cell adhesion strength, stronger polarity alignment corresponds to strong alignment of protrusion force in one direction that overcomes protrusion forces in other directions, resulting in the whole tumor moving in one direction.

Taken together, sufficient protrusion force is necessary for any kind of migration to occur, while strong cell-cell adhesion is necessary for directional migration.

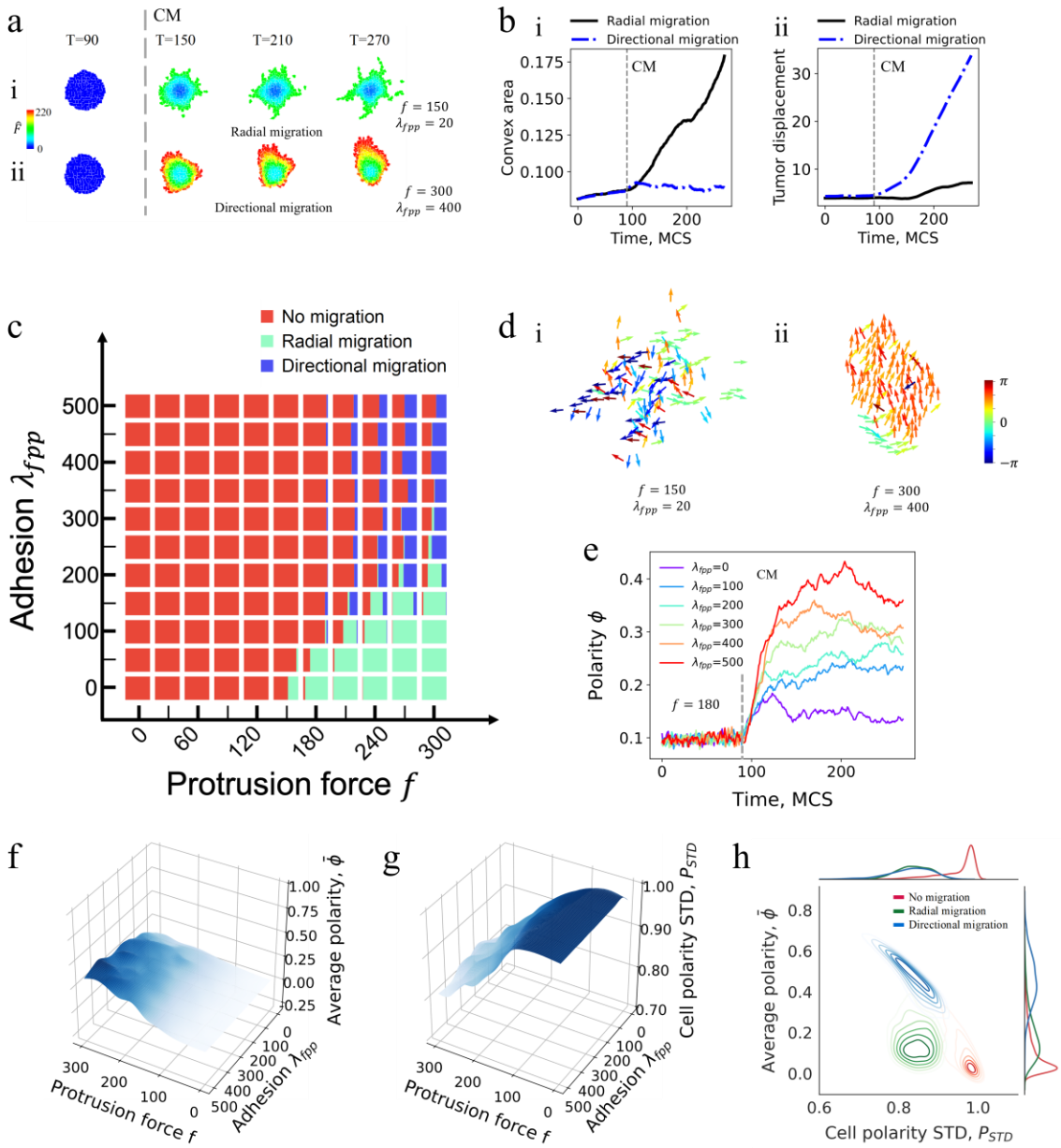

Figure 3. The multiscale microtumor model recapitulates distinct migration modes. **a.** Representative snapshots showing (i) radial migration with $f = 150$ and $\lambda_{fpp} = 20$ and (ii) directional migration with $f = 300$ and $\lambda_{fpp} = 400$. **b.** Temporal trajectories for (i) convex hull area and (ii) tumor displacement corresponding to those in panel a. The x-axis is time in Monte Carlo steps (MCS). **c.** Fractions of the tumors showing different migration modes in the parameter space of protrusion force f and adhesion strength λ_{fpp}. **d.** Representative tumor cell polarity snapshots for (i) radial migration and (ii) directional migration for two simulations in panel a. **e.** Representative time trajectories for tumor polarity for varying adhesion strength λ_{fpp}, with $f = 180$. **f.** Average tumor polarity $\bar{\phi}$ shows high average polarity for high protrusion force f and high adhesion λ_{fpp}. **g.** The variance of cellular polarity P_{STD} decreases as protrusion force f increases, while adhesion strength λ_{fpp} has less impact on P_{STD} compared to the protrusion force f. **h.** Gaussian kernel density estimation (KDE) plot for distribution of tumor migration modes in the parameter space of cell polarity variance P_{STD} and tumor average polarity $\bar{\phi}$. The levels for kernel density are $[0.2, 0.4, 0.6, 0.8]$.

4. Reducing protrusion force attenuates radial tumor migration.

We next sought to understand the impact of protrusion force on tumor migration. In MSMM, force f exerted in single cells is regulated by a general force regulator $[R]$, under the influence of the secretome. We examined distribution of tumor migration modes by varying maximum protrusion force f, at constant cell-cell adhesion strength at $\lambda_{fpp} = 50$ **(Figure 4a**). With this relatively low cell-cell adhesion strength, tumors either remain non-migratory or exhibit radial migration recapitulating our experimental observation of radially migrating 150CM microtumors after CM treatment [21, 23]. With an increasing protrusion force, the dominant migration mode changed from non-migratory to radial migration (**Figure 4a**), where the percentage of radially migrating tumors increased with increasing protrusion force. For example, with a stronger protrusion force $f = 200$, the tumor has a strong radial migration phenotype, showing strands extending in all random directions (**Figure 4b**). The convex area of microtumors, A_{tumor} (normalized by the total simulation area, **Supplementary Table S3**) and cell displacement distance, $\bar{d}$ (measured from the initial tumor center, **Supplementary Table S3**) both increased with stronger protrusion force (**Figure 4c and 4d**).

Many factors can affect the protrusion force. Both pushing (protrusive) and pulling (contractile) forces are critical for cell migration [42, 43]. A pushing force, generated by coordinated polymerization of actin filaments, can be regulated by Rac1 amongst many other factors. On the other hand, a pulling force can be generated by sliding actin filaments along myosin II filaments [42]. Myosin II, a key effector for Rho kinase signaling [44], is able to promote contractility and generate protrusion force by forming actomyosin filaments [45-47]. Abhinava *et al.* reported that myosin II regulates protrusion dynamics and can convert border cells into migratory cells in collective migration [48]. The functionality of myosin II has been extensively studied *in vitro* and *in vivo*. Therefore, we experimentally inhibited myosin II with blebbistatin treatment (**Figure 4e**).

When treated with blebbistatin, 150CM microtumors showed a significant reduction in the extent of migration (**Figure 4f-h**). Since we counted all the tumors that migrated out of the microwells as 'radially migrating' tumors irrespective of their extent of migration, we did not observe a significant reduction in the percentage of migrating tumors in the blebbistatin treated group (36.5± 14.6%) compared to the untreated 150CM microtumors (57.5 ± 11.2%) (p value=0.0755; paired t-test; n = 4 devices each containing approximately 480 microtumors from two independent biological experiments) (**Figure 4g**). However, distance of tumor migration showed a significant decrease in blebbistatin-treated tumors, while untreated 150CM tumors continued to migrate out of the microwell from day 4 to day 6. Indeed, the distance of migration reduced from 184 ± 44 µm for untreated 150CM microtumors to 78 ± 10 µm for blebbistatin-treated 150CM microtumors on day 6 (**Figure 4h**), suggesting inhibition of migration due to myosin II inhibition. This observation was further confirmed by reduced myosin light chain (MLC) expression in blebbistatin-treated microtumors compared to untreated control (**Figure 4i**). Taken together, our experimental results confirmed our model prediction that reduced protrusion force reduces radial migration.

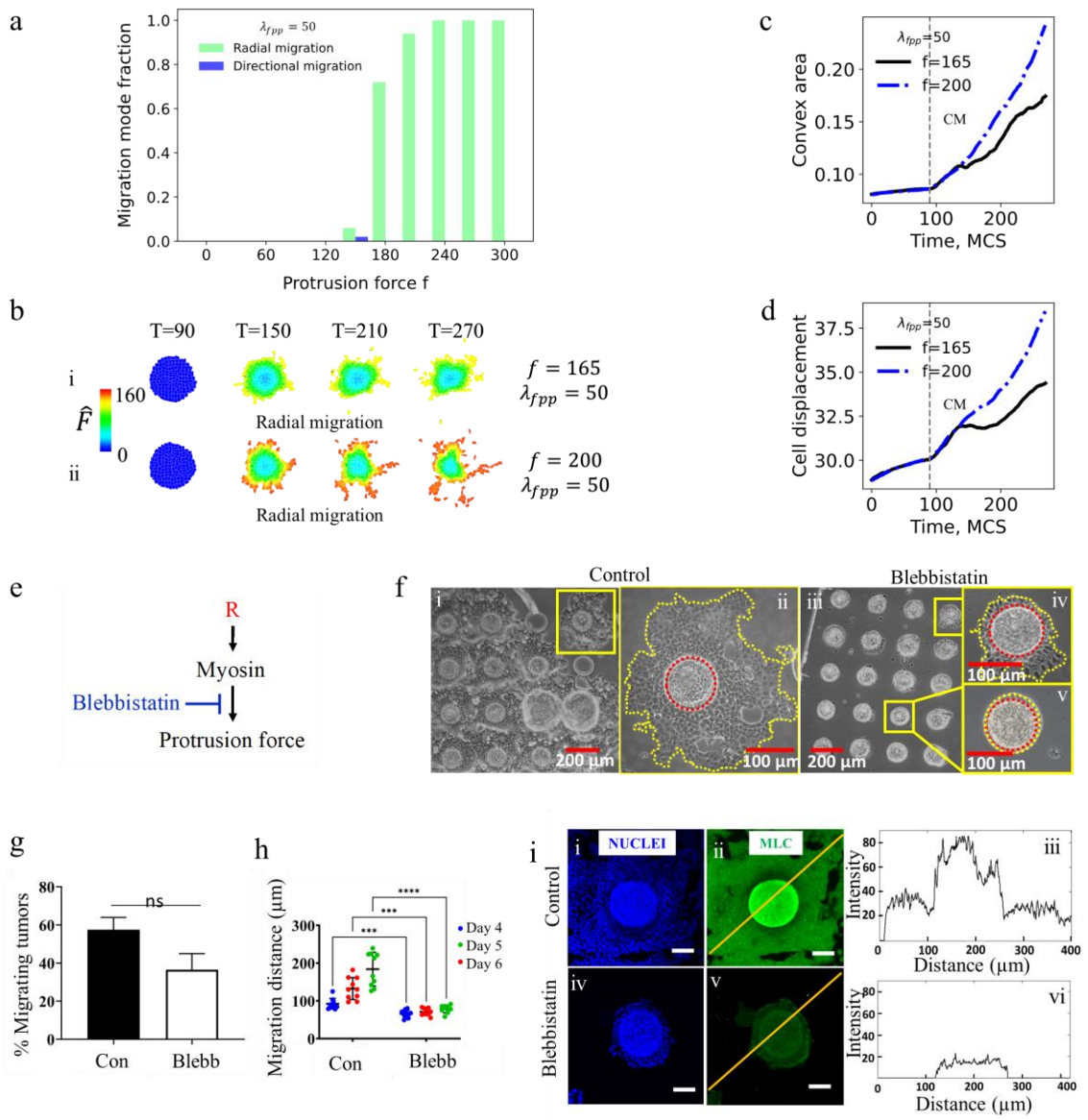

Figure 4. Reducing protrusion force attenuates radial tumor migration. **a.** Distribution of fraction of tumor migration modes as a function of varying protrusion force in the parameter scan with constant adhesion strength $\lambda_{fpp} = 50$. **b.** Typical time trajectories for simulation with (i) weak (*f* = 165) and (ii) strong (*f* = 200) protrusion force at a constant adhesion strength of $\lambda_{fpp} = 50$. The single cell protrusion force $\hat{F}$ is color coded. The time trajectories for **c.** convex area and **d.** average cell displacement from the initial center of the tumor with weak (black line) and strong (blue) protrusion force are shown. The x-axis is time in Monte Carlo steps (MCS). **e.** Inhibition of myosin II by blebbistatin impairs generation of protrusion force. Panels **f-h** show the effect of myosin inhibition on 150CM tumors using blebbistatin treatment. f. Brightfield images showing significantly reduced distance of migration in (iii-v) blebbistatin-treated 150CM tumors on day 6 compared to (i-ii) untreated control. **g.** Percentages of migrating tumors did not decrease significantly on day 6 in blebbistatin-treated group compared to the control (*p-value* = 0.0755; paired t-test; *n* = 2 devices each containing 484 microtumors from two independent biological experiments). **h.** Extent of migration reduced significantly in 150CM microtumors in blebbistatin-treated microtumors compared to the untreated control. (*p-value* <0.0005, two-way ANOVA, *n* = 10 representative microtumors, N = 2 devices). **i.** Confocal microscopy images of control and blebbistatin-treated microtumors after immunostaining with Hoechst

(nuclei; blue) and myosin light chain (MLC; green) antibody. The myosin light chain (MLC) expression is reduced in the blebbistatin-treated microtumor (iv-v) compared to the untreated control (i-ii). The respective intensity plot profiles indicate decreased intensity of MLC and reduced extent of migration in the blebbistatin-treated microtumors compared to the control.

5. Increased cell-cell adhesion decreases radial migration while promoting directional migration.

Directional migration was first observed in large microtumors under tumor-intrinsic hypoxia conditions. Our RNA microarray analysis revealed key directional migration gene signatures, including PIK3R3 [23], a regulatory component for PI3K. Interestingly, PI3K-AKT pathway was also found to be differentially regulated in directional and radial migration modes by pathway enrichment analysis. AKT, the serine/threonine protein kinase, plays important roles in PI3K/AKT pathway, regulating cell metabolism, growth, proliferation, and survival [49]. PI3K activates AKT [3], and the latter is composed of three isoforms, AKT1, AKT2, and AKT3 [50]. Several studies have established that the isoforms, AKT1 and AKT2, play distinct and opposing roles in cell signaling and tumor growth and progression [51-53]. A study by Polytarchou *et al.* [54] further elucidated association between AKT and hypoxia, and reported that only AKT2 is induced under hypoxic conditions and not AKT1 or AKT3. Also, AKT2 expressing cells were more resistant to hypoxia-mediated cell death and hypoxia-induced cell cycle G1/S arrest. Furthermore, under oxygen deprivation, AKT2, via PTEN inhibition, acts as a master regulator of all three isoforms of AKT, which ensures higher survival of cells under hypoxia [54]. Among AKT isoforms, our microarray analysis revealed that AKT2 is differentially regulated in hypoxia-induced directional migration and secretome-induced radial migration [23]. Since role of AKT2 in 3D collective migration remains understudied, we further studied the effect of AKT2 inhibition on 150CM microtumor migration.

Upon treatment with CCT128930, a potent AKT2 inhibitor, the percentage of migratory microtumors (16.4 ± 3.9) reduced significantly (p value= 0.01) compared to untreated 150CM

group (40.1 ± 12.6) (**Figure 5a-b**). Note that we counted all the tumors that migrated out of the microwells as 'migrating' tumors irrespective of their extent of migration. For the migratory tumor population in the CCT128930-treated group, we did not observe significant changes in the extent of migration except on day 6 compared to untreated control (**Figure 5c**). Within the CCT128930-treated group, in addition to complete inhibition of migration, 10.9 ± 5.6% tumors continued to migrate radially. Interestingly, we observed emergence of a directional migration phenotype in 5.5 ± 2.2% microtumors with AKT2 inhibition (**Figure 5a-b**). These data suggest that AKT2 plays a role in determining the mode of migration. This was further confirmed by the differential expression of pAKT in the radial and directional migration modes, while the expression of total AKT remained unchanged (**Figure 5d**). Our experimental results suggest that AKT2 may play an important role in the plasticity of collective migration modes of microtumors.

The cell-cell adhesion plays a central role in cell migration [55]. AKT2 may regulate microtumor migration by tuning cell-cell adhesion. For example, cell adhesion pathways are reported to be upregulated in AKT2 knockout cells [50]. E-cadherin is a key cell adhesion molecule mediating adherens junction and maintaining epithelial phenotype of cells [56]. Indeed, Snail1 has been shown to interact with AKT2 in the CDH1 promoter and reduce E-cadherin expression, thus explaining pro-mesenchymal role of AKT2 [56]. Ectopic Snail1 expression has also been shown to promote AKT2 kinase binding to CDH1 promoter, thus decreasing E-cadherin expression [57, 58]. The mechanistic role of cell-cell adhesion in the plasticity of tumor migration modes remains elusive. It is also challenging to precisely measure the cell-cell adhesion strength experimentally.

Our MSMM described above takes into account the critical role of cell-cell adhesion in directional tumor migration. The MSMM model simulations suggest that increasing cell adhesion strength leads to emergence of directional migration (**Figure 3c**). Thus, we examined distribution of tumor migration modes as a function of adhesion strength λ_{fpp} with maximum protrusion force fixed at $f = 210$ (**Figure 5e**). At a lower adhesion strength $\lambda_{fpp} \leq 100$, most tumors migrate radially.

Increasing adhesion strength λ_{fpp} leads to a decrease in the fraction of radially migrating tumors. At $\lambda_{fpp} \geq 100$, directional tumor migration emerges. Thus, the MSMM simulations show that increasing cell-cell adhesion can switch the microtumor migration from radial to directional migration.

Figure 5f-h shows example trajectories from simulations with different adhesion strengths. At a low adhesion strength, where λ_{fpp} = 50, tumors migrate radially. At a moderate adhesion strength, where λ_{fpp} = 130, two modes of migration, *i.e.*, radial and directional migration mode, co-exist. At a high adhesion strength, where λ_{fpp} = 400, directional migration mode predominates. Two geometric features, the average cell displacement $\bar{d}$ and tumor displacement D_{tumor} (displacement of tumor centroid, **Supplementary Table S3)** are shown in **Figure 5i-j**. We compared typical time series for cell displacement and tumor displacement under weak ($\lambda_{fpp} = 50$, red line), moderate ($\lambda_{fpp} = 130$, green lines), and strong ($\lambda_{fpp} = 400$, purple lines) adhesion strength conditions, and found that the directional migration has distinct properties compared to the radial migration mode in terms of cell displacement and tumor displacement (**Figure 5i-j**). In **Figure 5i**, after treatment with CM, cell displacement of non-migratory tumors keeps steady at lower values, while the cell displacement keeps increasing in directional and radial migratory tumors. In **Figure 5j**, after treatment with CM, tumor displacement of directionally migrating tumors increases, while the tumor displacement of radial and non-migratory tumors remains steady near 0 during the simulation. These observations from the MSMM simulations verified the co-existence of directional migration and radial migration in moderate adhesion conditions, and that directional migration and radial migration possess distinct properties during the simulation.

To summarize, AKT2 inhibition studies (**Figure 5a-d**) revealed an important role of AKT2 in regulating the plasticity of microtumor migration modes, while the MSMM can recapitulate the observed plasticity of collective migration by varying cell adhesion strength. Taken together, we

postulate that AKT2 is a critical regulating factor in determining the plasticity of collective migration by regulating adhesion-related biophysical properties.

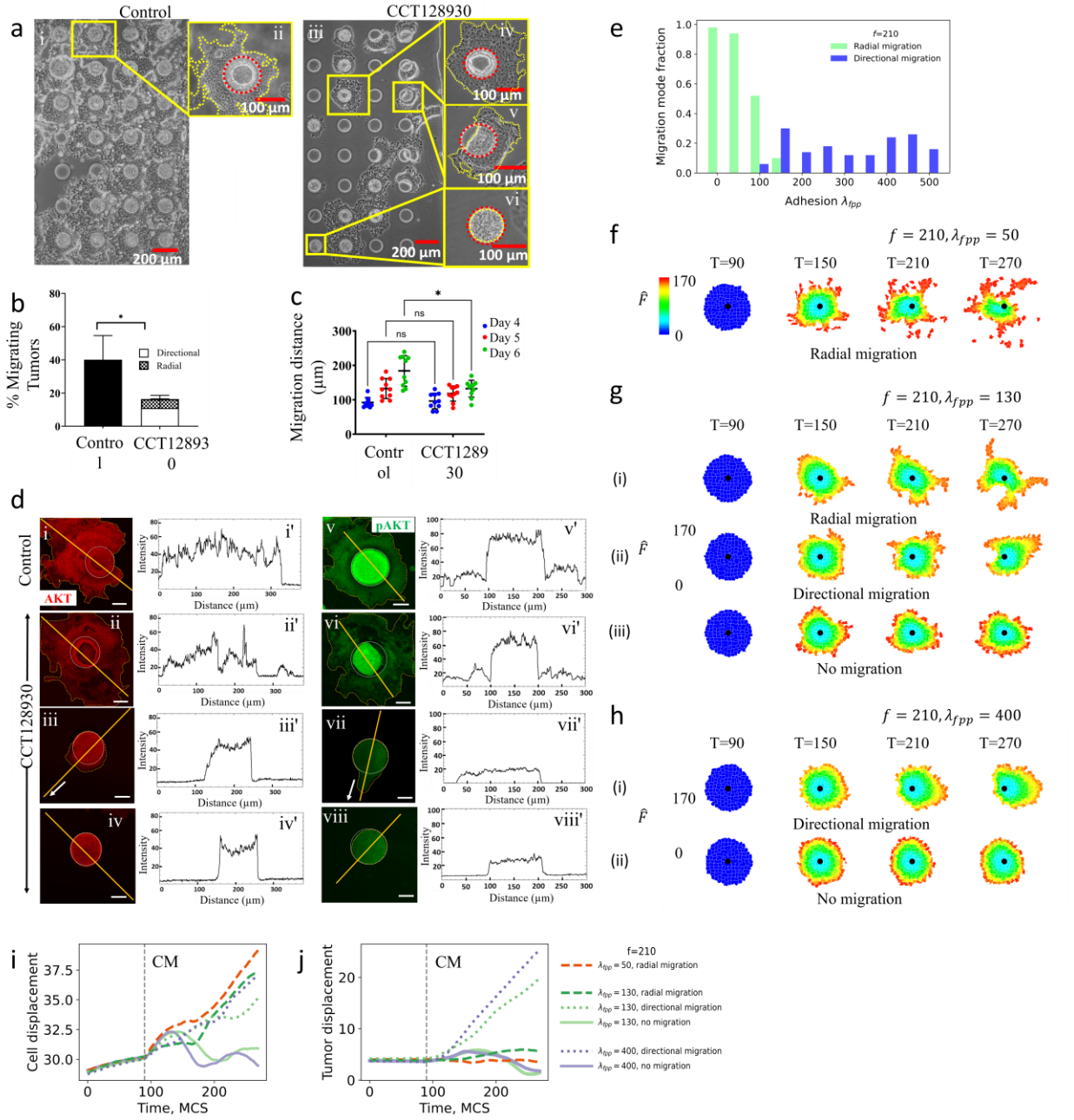

Figure 5. Increased cell-cell adhesion decreases the fraction of radially migrating tumors and promotes directional migration. **a.** Brightfield images showing dominance of radial migration in untreated controls (i & ii) whereas CCT128930-treated150CM tumors (iii) consist of a mixed population of (iv) radially migrating, (v) directionally migrating, and (vi) non-migratory tumors on day 6. **b.** Percentages of migrating tumors in CCT128930-treated group decreased significantly on day 6 compared to the untreated control group ('*' denotes *p* value of 0.01; paired t-test, n=2 devices each containing 484 tumors). We observed a mixed population of migrating tumors displaying either radial or directional mode of migration. **c.** Treatment with

CCT128930 significantly reduced the extent of migration compared to the untreated control on Day 6 (*p* value = 0.018, two-way ANOVA, *n* = 10 different microtumors, N = 2 independent experiments). **d.** Confocal microscopy images of control and CCT128930-treated microtumors after immunostaining for total AKT (red) and pAKT (green) (Scale bar = 50µm). Arrows represent the direction of migration. Differential expression of pAKT was observed in CCT128930-treated tumors when compared to the control group, while expression levels for total AKT remained unchanged. The respective intensity plot profiles for each image were plotted in ImageJ (i - viii). **e.** At a constant protrusion force $f = 210$, distribution of tumors in different migration modes (radial versus directional) is dictated by the cell-cell adhesion strength λ_{fpp}. Radial migration mode dominates at low cell-cell adhesion ($\lambda_{fpp} \leq 100$) values (weak cell-cell adhesion) while strong cell-cell adhesion ($\lambda_{fpp} > 100$) promotes directional migration. The total fraction of both, radial and directional migratory tumors is also reduced as the cell-cell adhesion strength increases. **f.** Typical simulation time snapshots show radial migration in low adhesion conditions ($\lambda_{fpp} = 50$). Black dots are initial tumor centers. **g.** Under moderate cell-cell adhesion strength $\lambda_{fpp} = 130$, time snapshots for three typical migration modes, (i) radial, (ii) directional, and (iii) non-migratory modes are shown. **h.** Under strong cell-cell adhesion strength $\lambda_{fpp} = 400$, (i) directional migration and (ii) non-migratory modes coexist, and their typical migration time snapshots are shown. **5i** and **5j** show examples of simulated trajectories for cell displacement and tumor displacement under varying cell-cell adhesion strength. The x-axis is time in Monte Carlo steps (MCS).

Discussion

Collective migration of cells is a hallmark of many physiological and pathological processes such as embryonic morphogenesis, wound healing, and stage IV cancer progression [46]. In cancer metastasis, collective migration confers higher invasive capacity and resistance to therapy compared to single-cell migration [59, 60]. Clinically, circulating tumor cell (CTC) clusters, prevalent in metastatic patients, exhibit increased resistance to radiotherapy and chemotherapy [59, 61-63] and are often associated with worse prognosis [64]. Collectively migrating tumor clusters exhibit improved cell survival in various microenvironments, evade the immune system and colonize secondary sites more efficiently [64]. Furthermore, different tumor cells exhibit migratory plasticity, which refers to the ability of tumor cells to reversibly switch between different migration modes, depending on the cellular and microenvironmental context [65-68]. Such plasticity adds further complexity to tumor migration mechanisms, necessitating a fundamental perspective model for comprehensive understanding. Here, we employed experimental 3D microtumor models [18-23] and computational modeling to elucidate the mechanisms underlying collective migration in secretome induced microenvironments. Notably, our multiscale modeling approach integrated single-cell signaling with population-level interactions, focusing on the dynamic interplay between cellular protrusion force and cell-cell adhesion.

Widely studied individual cell migration modes include mesenchymal, which mainly depends on the activity of small GTPase Rac, while amoeboid migration is mainly regulated by Rho-ROCK-MLCKII pathway [65, 69]. While many molecular signature and pathways have been investigated to understand the pathology in single cells [70, 71], the mechano-mechanisms for collective migration of microtumor clusters are less understood. We utilized our previously published [18-23] 3D microtumor models where we observed collective directional migration in large microtumors in response to the tumor-intrinsic hypoxia and radial migration in small microtumors in response to the hypoxic secretome [21]. By analyzing RNA microarray data for these

microtumors, we identified key molecular signatures of collective cluster migration, notably, differential regulation of AKT2 in hypoxia-induced directional migration and secretome-induced radial migration [23]. In addition, GO term enrichment analysis of differentially expressed genes revealed upregulation of cell-cell adhesion in directional migration while actin-microtubule cytoskeleton reorganization was upregulated in radial migration. Based on the analysis results, we built a minimal multi-scale microtumor model (MSMM) focusing on the cell-cell adhesion and protrusion force to recapitulate the observed emergence of directional and radial migration.

The multi-scale microtumor model (MSMM) recapitulate both migration modes observed experimentally in microtumors and provide insight into the mechanism underlying the plasticity of tumor migration modes. MSMM provides quantitative measurements and time series for microtumor geometric features, such as tumor polarity, tumor convex area, tumor displacement distance, cell displacement distance, and classifying tumor migratory phenotypes in morphological space with machine learning methods. With the parameter scan, we found that the sufficient protrusion force is necessary for tumors to migrate, consistent with the previously published reports [39, 72, 73]. Radial migration emerges when sufficient cellular protrusion force is generated, propelling neighboring cells to migrate collectively in diverse directions. Within migrating tumors, stronger cell-cell adhesion intensifies the alignment of cell polarity. This intensified alignment breaks the symmetric angular distribution of protrusion forces, leading to directional tumor migration. This result is consistent with findings on collective cluster migration that requires coordination between single cells [74, 75]. Our results show that radial migration emerges under sufficient protrusion force and weak adhesion, while directional migration mode emerges under relatively strong adhesion with sufficient protrusion force. Clustering tumor migration modes by morphological features is a novel approach for machine learning in cancer research.

To corroborate our findings from the computational model, we conducted myosin II inhibition experiments to confirm the role of protrusion force in microtumor migration. Myosin II is a motor protein that is responsible to convert chemical energy into mechanical energy, generating force and movement [39, 48, 76-79]. We observed that inhibiting myosin II reduced radial migration of microtumors, but didn't change the migration modes, echoing with our MSMM simulation results.

We then explored AKT2 as a signature regulating cell-cell adhesion and contributing to the emergence of directional migration. In microarray analysis, PIK3R3 was established as the molecular signature of directional migration in hypoxia induced microtumors [23], which is a part of the PI3K-Akt pathway [49]. Its downstream protein AKT2 plays a central role in cell migration and invasion [54], and is differentially regulated in hypoxia-induced directional migration and secretome-induced radial migration [23]. Pharmacological inhibition of AKT2 resulted in transition from radial migration to directional migration mode, which was also recapitulated in MSMM simulation by increasing cell-cell adhesion strength. It is technically difficult to quantify cell-cell adhesion strength directly. However, our integrated results from the ATK2 inhibition experiment and the MSMM simulations suggest that the AKT2 functions as a cell-cell adhesion regulator, which can be supported through prior literature. Indeed, AKT2 has been shown to bind to CDH1 promoter and repress E-cadherin expression [57, 58], important in maintaining cell-cell adhesion and connecting with the cortical actin cytoskeletons of cells [32, 80]. Strong cell-cell adhesion can contribute to directional migration due to improved cell clustering in bloodstream [81] and more efficient cell-cell communication by passing signaling molecules to neighboring cells via gap junctions [82-84], which can help adapt gene expression to selective pressure, such as oxidative stress and fluidic shear stress in a local microenvironment [64, 85, 86]. E-cadherin is known as a tumor suppressor, but also functions as a promoter of growth and metastasis, based on local cellular and microenvironmental context [68, 87-91]. Further investigation is needed to understand

the mechanistic link between AKT2 and E-cadherin to regulate cell-cell adhesion changes. Such insights can be exploited for potential therapeutic targeting.

Despite its advantages, MSMM also has disadvantages. Currently, the minimum model does not include cell growth and cell death, which could be implemented carefully in the future. Cell growth and death may introduce additional complexity, as Janet *et al* mentioned that mechanical compression may correlate with invasive phenotypes [79], and mechanical compression from growth may also reduce cell growth rate [92, 93]. The model can be further improved by considering tumor size effects. Tumor size may impact the dynamics, such as intrinsic hypoxia-induced cell death in the tumor center, ROS stress signaling pathways activation, and hypoxia driven polarity changes [94]. While MSMM has the advantage of providing detailed insight into biophysical quantities that otherwise cannot be measured, such as cell-cell adhesion strength, it can be further expanded and adapted to different scenarios. For example, the model can incorporate more complex regulatory networks into its single cell dynamics with ordinary differential equations (ODE). Overall, a thorough model would be needed to understand mechanisms in depth such as regulation of signal molecules, effect of tumor size and growth rate on microtumor migration.

To summarize, we provide a mechanistic framework of interplay between protrusion force and cell-cell adhesion for understanding collective migration of microtumors using integrated experimental and computational approaches. Protrusion force is an essential driver for collective metastasis, and stronger cell-cell adhesion influences alignment of cell polarity leading to directional migration. In-depth understanding of underlying mechanisms of plasticity of tumor migration could guide design of combination drug therapy to prevent collective migration.

Acknowledgement

This work was supported by National Cancer Institute (R37 CA232209, to SS and JX), National Institute of General Medical Sciences (R01GM148525 to JX), National Science Foundation

(DMS2325149 to JX), and National Eye Institute (R01EY028450) and the endowment for Frady Whipple Chair at Georgia State University (to YJ). This research was supported in part by the University of Pittsburgh Center for Research Computing through the resources provided. Specifically, this work used the H2P cluster, which is supported by NSF award number OAC-2117681. We also thank Drs. James A. Glazier, James P Sluka, T.J. Sego, and Juliano Ferrari-Gianlupi for help with Compucell3D, and Dr. GW McElfresh for help in mathematics.

Supplementary Materials

Materials and methods

Cell lines and cell culture

The T47D breast cancer cell line (RRID:CVCL_0553) was purchased from American Type Culture Collection (ATCC). Media for cell culture was obtained from Corning® unless specified. The cells were passaged and maintained in T75 flasks using Dulbecco's modified Eagle's medium (DMEM) (MT10013CV, Corning®, VA, USA) supplemented with 10% fetal bovine serum (FBS) (S11250, Atlanta biologicals, GA, USA), and 1% penicillin-streptomycin (300-002-CI, Corning®, VA, USA) in a humidified atmosphere at 37°C and 5% CO2. Cells were maintained between 60-70% confluency for further passaging or seeding into hydrogel microwell devices. Cell line authentication was done by the University of Arizona, Genetics Core (UAGC) by using PowerPlex16HS PCR Kit as previously described [21].

Microtumor fabrication

Uniform-sized microtumors of 150 µm diameter were fabricated by seeding T47D cells in Polyethylene glycol dimethacrylate (PEGDMA) hydrogel microwell devices as previously described [18, 19, 21, 22]. Briefly, polydimethylsiloxane (PDMS) stamps (1x1 cm^2) containing posts of 150 µm in diameter and 150 µm in height were used to produce microwell devices. A solution of polyethylene glycol dimethacrylate (20% w/v, PEGDMA, 1000Da, Polysciences Inc, USA) containing photoinitiator (Irgacure-1959, 1% w/v, Ciba AG CH-4002, Basel, Switzerland) was crosslinked under the PDMS stamps using OmniCure S2000 curing station (200W Lamp, $5W/cm^2$, EXFO, Mississauga, Canada). The fabricated microwell hydrogel devices were sterilized by submerging them in 70% ethanol under UV light for 1h. Sterilized hydrogel devices were then washed three times with Dulbecco's phosphate buffered saline (DPBS) without calcium and magnesium (Corning™, USA, catalog #21-031-CV). For cell seeding, a suspension of 1 $x10^6$

T47D cells (RRID:CVCL_0553) in 50 µL of growth media was dropped on each hydrogel microwell device. Cells were allowed to settle in the microwells for 15 min. The cells that did not settle into the microwells were removed by gentle washing with DPBS. The cell-seeded devices were cultured at 37 °C and 5% CO2 in a humidified incubator. On day 1 and day 2, 50% of the culture media was replaced with an equal volume of fresh media. To study migration induced by tumor secreted factors, 150µm microtumors were treated with conditioned media (CM) from hypoxia-rich larger (600µm) microtumors starting from day 3 until day 6 (referred to as **150CM** hereafter), with the replacement of 50% media with an equal amount of CM every day as described in our previous studies [21]. Control 150µm microtumors (referred to as **150** hereafter) were cultured similarly for 6 days with a replacement of 50% media with fresh media every day and these microtumors served as non-migratory controls.

Assessment of microtumor migration

The aggressiveness of the migratory phenotype of microtumors was assessed by quantifying the percentage of migrating tumors of each microwell hydrogel device (n=3), and the distance of migration. The distance of migration was estimated in ImageJ (RRID:SCR_003070)by measuring the average length of at least 10 straight lines drawn perpendicular to the boundary of the well up to the leading edge of the microtumor, covering the entire migratory front of at least 10 migrating microtumors per group.

Microarrays and bioinformatic analysis

Microarray data was collected as described previously [23]. Briefly, at the end of six day culture, RNA was isolated from 150D6 (control non-migratory microtumors) and 150CM microtumors using GenElute™ Mammalian Total RNA Miniprep Kit (cat #RTN70-1KT) and DNA cleanup was done by On-Column DNase I Digestion Set (Cat#DNASE70-1SET) as per manufacturer's protocols. RNA quantity was measured by absorbance ratio at 260/280 nm and integrity was verified on 1% agarose gel. cDNA preparation, hybridization to GeneChips, scanning, and first

level data analysis was performed at the University of Pittsburgh HSCRF Genomics Research Core as described previously [23]. Microarray data is deposited in the Gene Expression Omnibus database at the National Center for Biotechnology Information (GSE166211, RRID:SCR_005012). Differential gene expression in migratory 150CM induced by secretome was analyzed by normalization with the 150D6 (150CM *versus* 150D6). Transcriptome Analysis Console (TAC 4.0, ThermoFisher Scientific, MA, USA) was used to perform statistical analysis on the comparison using one-way ANOVA. The initial assessment of the microarray expression data was performed by hierarchical clustering using a cut-off *p*-value of 0.01. All the genes with False Discovery Rate (FDR) ≤ 0.05, *p-value* ≤ 0.05, and fold change ± 2 were considered significantly different in terms of gene expression and were selected for further analysis. Gene Set Enrichment Analysis (GSEA) was carried out for Gene Ontology (GO) enrichment of Biological Processes (BP) using the GSEA software with minimum size cut off =5 (UC San Diego and Broad Institute, San Diego, CA, USA) as discussed previously [23]. We performed analysis of differentially enriched GO: BP related to '*actin polymerization*', '*cell-cell adhesion*', '*cell junction*', '*adherence junction*', '*cell polarity*', and '*cytoskeleton reorganization*' to capture phenotypic differences in directionally migrating 600D6 and radially migrating 150CM microtumors compared to non-migratory 150 µm microtumors.

Microtumor inhibition studies

Based on our microarray data analysis, we used inhibitors of myosin and AKT2 molecules to investigate their role in the development of collective migration phenotypes. All the inhibition treatments started on Day 3 along with the first supplement of CM. Myosin light chain (MLC) inhibition was achieved by treating 150CM microtumors with 50 µM of Blebbistatin (# 50-101-3165, Apexbio Technology LLC, cat). Blebbistatin is a cell permeable, selective pharmacological inhibitor of myosin II [77, 95] Complete solubilization of Blebbistatin in either growth media or CM was achieved by 2h sonication in an ultrasonic bath at 37°C and 40kHz. AKT Serine/Threonine Kinase 2 (AKT2) was inhibited chemically by the treatment of 150CM microtumors with growth

media CM containing CCT128930 (# 50-190-5165, Apexbio Technology LLC) at a final concentration of 25 µM. CCT128930 is an ATP-competitive selective pharmacological inhibitor of AKT2 and its downstream targets [96, 97]. Untreated 150CM microtumors were used as controls.

Immunostaining and confocal microscopy

Microtumors were fixed with 4% paraformaldehyde, permeabilized with 0.1% Triton X-100 in 1X PBS, and blocked with 3% BSA in 1X DPBS containing 0.1% Triton X-100. Microtumors were stained for myosin light chain (MLC) (#109061-1-AP, Proteintech), AKT (#4691; Cell Signaling Technol32hosphornd phospho-AKT (pAKT) (#4060; Cell Signaling Technology) by incubating the samples with respective primary antibodies overnight at 4ºC. Samples were then washed with 1X DPBS and incubated with secondary antibody Alexa Fluor 488 goat anti-rabbit (#A11008, Invitrogen) for 2h. Samples were washed again with 1X DPBS and incubated with a Hoechst solution in 1X DPBS for 24h. The stained samples were washed with 1X DPBS and mounted in glycerol on microscopy slides (#6776214, Thermo Scientific). Confocal imaging was carried out on the Olympus FV1000 inverted confocal microscope at the University of Pittsburgh, Department of Pharmaceutical Sciences, using a step size of 5 µm. Maximum intensity Z-projections and intensity plot profiles were generated using FIJI software (ImageJ) (RRID:SCR_002285 and RRID:SCR_003070).

Statistical Analysis

All the values are presented as mean ± standard deviation. Paired t-test was used for statistical comparisons between inhibitor-treated and untreated control groups. Two-way ANOVA was used to compare the level of significance in the extent of microtumor migration between the inhibitor-treated *versus* untreated control group. Sample sizes for each study were indicated in the respective figure legends. A *p*-value less than 0.05 was considered significant.

Multi-scale microtumor model energy terms

In the multi-scale microtumor model, cells move by random attempts of copying their lattices to neighboring lattices. The MSMM represents cells on a 256×256 lattice, where cells are represented as a set of pixels, and different cells do not overlap. Each cell is constrained with surface energy, boundary energy and energy from protrusion force (**Supplementary Table S1**). A global effective energy H consists of cell constraints, such as area and perimeter, cell-cell interactions, cell-medium interactions, and protrusion force energy. The Hamiltonian H function is defined as:

$$H = H_{shape} + H_{surface} + H_{adhesion} + H_{protrusion}. \tag{S1}$$

The term H_{shape} comes from cell shape constraints and is defined as:

$$H_{shape} = \lambda_{area} \sum_{\sigma=1}^{N} (a_\sigma - A_\sigma)^2 + \lambda_{peri} \sum_{\sigma=1}^{N} (l_\sigma - L_\sigma)^2 , \tag{S2}$$

where λ_{area} and λ_{peri} are parameters that describe cell elasticity. The σ is the cell identity. The total number of cells in the simulation is N. a_σ and l_σ are the area and perimeter for cell σ, and A_σ and L_σ are the target area and perimeter corresponding to a_σ and l_σ.

The second term, $H_{surface}$ in Eq. S1, describes the surface properties for cell-cell, cell-medium and medium-medium contacts as:

$$H_{surface} = \sum_{i,j} J(\sigma_i, \sigma_j) \left(1 - \delta(\sigma_i - \sigma_j)\right). \tag{S3}$$

The indices i and j are neighboring lattices, σ is the cell identity, and the total number of cells in the simulation is N. $J(\sigma_i, \sigma_j)$ is the interface energy function defined in the model, and the term $\delta(\sigma_i - \sigma_j)$ is Kronecker delta that only allows interactions between pairs of different lattices.

The third term on the right-hand side of Eq. S1, $H_{adhesion}$, describes the adhesion energy, defined as:

$$H_{adhesion} = \lambda_{fpp} \sum_{\sigma=1}^{N} \sum_{\omega=1}^{M} (\mathrm{d}_{\sigma\omega} - \mathrm{D}_{\sigma\omega})^2 . \qquad (S4)$$

The $H_{adhesion}$ represents adherens junctions (AJ) that link cells; disrupting the AJs results in loss of cell-cell contacts. In cancer cells, catenins in the cytoplasm bind to cytoskeletal components, such as actin filaments and microtubules to form AJs [98]. This adhesion linkage is described as strings that link cell centers, using the FocalPointPlasticity (FPP) plugin in CompuCell3D (RRID:SCR_003052). For cell σ, M is the number of neighboring cells for σ. The $\mathrm{d}_{\sigma\omega}$ is the distance between the centers of mass of cells σ and ω, and $\mathrm{D}_{\sigma\omega}$ is a target length corresponding to $\mathrm{d}_{\sigma\omega}$. λ_{fpp} is a constraint parameter that describes the strength of the focal point links.

The last term, $H_{protrusion}$ in Eq. S1 describes the energy term simulating protrusion force:

$$H_{protrusion} = -\sum_{i,j} \vec{\mathrm{F}}_{\sigma_i} \vec{\mathrm{r}}_{ij} , \qquad (S5)$$

where $\vec{\mathrm{F}}_{\sigma_i}$ is the protrusion driving force for attempt copy from pixel i to j for cell σ, and $\vec{\mathrm{r}}_{ij}$ is the distance vector [99]. $\vec{\mathrm{F}}_{\sigma_i}$ is regulated by single cell protrusion force regulator R, and its mathematical expression is given later (Eq. S10).

Conventionally, the multi-scale microtumor model (MSMM) accepts a Monte Carlo move for lattice u copy to v with the Boltzmann probability $p(u \to v)$ as shown in Eq. S6

$$p(u \to v) = \begin{cases} 1 & if\ \Delta H < 0 \\ e^{-\frac{\Delta H}{T}} & if\ \Delta H > 0 \end{cases} , \qquad (S6)$$

Where, $\Delta H = H_v - H_u$ is the attempted move contribution to total effective energy. The effective temperature $T(> 0)$ is a parameter to control the move acceptance probability, with the

acceptance probability $p(u \to v)$ increases as T increases. We use a constant $T = 25$ for all simulations.

Secretome signals diffuse into tumor cells

Secretome induces radial migration for 150μm microtumors (**Figure 1b**) by activating an unidentified protein regulator R. There are many potential candidate protein R that can regulate cell cytoskeleton remodeling and generating protrusion force, such as Rac1-GTP, a Rho GTPases family protein typically residing at the migration front regulates the formation of lamellipodia, or myosin II, a motor protein that binds F-actin to generate contraction force, and so on. For 150μm microtumors treated with the conditioned media (150CM) from hypoxic tumors, the secretome uptake is simulated as a diffusion field. The medium serves as the boundary for secretome signal field, where every pixel has a constant value of 1. The secretome signal diffuses into the tumor cells (both protrusive cells and non-protrusive cells), following the function for location $\vec{\mathrm{x}}$:

$$\frac{\partial c(\vec{\mathrm{x}}, t)}{\partial t} = D\nabla^2 c(\vec{\mathrm{x}}, t) - k_{uptake} c(\vec{\mathrm{x}}, t), \tag{S7}$$

where $c(\vec{\mathrm{x}}, t)$ is the concentration of secretome signal at position $\vec{\mathrm{x}}$ and time t. D is the diffusion coefficient, and k_{uptake} is the pixel-wise uptake rate by cell at position $\vec{\mathrm{x}}$ and time t.

Thus, for cell σ at the time t, the production rate s of protein R, which is dependent on single cell secretome signal, can be obtained by

$$s(\sigma, \mathrm{t}) = \zeta \frac{\sum_{i \in \sigma} k_{uptake} c(\vec{\mathrm{x}}, \mathrm{t})}{a_\sigma}, \tag{S8}$$

where i is lattice in cell σ, a_σ is the area for cell σ and ζ is a coefficient that constrains single cell $s(\sigma, t)$.

Secretome induces protrusion force regulator R

Protrusion force is the driving force for tumor migration [48, 78, 100]. In many studies, researchers define migration driving force as retraction force and protrusion force separately. In our model, we did not explicitly distinguish them. The protrusion force can point towards tumor center causing protrusion to retract or promote protrusion when pointing outwards. We have shown that the conditioned media from hypoxic microtumors induced migratory phenotype in the non-migratory 150μm microtumors [21]. To mathematically model this behavior, we hypothesize that a to-be-identified protrusion force regulator R, is induced by conditioned media from hypoxic tumors and is capable of mediating cell protrusion. In our multi-scale microtumor model, the production rate of the protrusion force regulator R is composed of a ubiquitous basal rate b and a secretome signal-induced activation rate s, where s is a fraction of uptake of secretome signal at single cell level, calculated from Eq. S8. In this way, the tumor cells at the boundary of the tumor in contact with the media receive more secretome signals than the tumor cells in the center of the tumor, and thus, will have higher R at the boundary. The spatial distribution of R is represented by the secretome-induced activation rate s. The R dynamics can be described as follows:

$$\frac{d[\mathrm{R}]}{dt} = b + s - d[\mathrm{R}] \tag{S9}$$

Where b is a basal production rate of R, independent of secretome signals in the microenvironment, with the unit of $\mu M/s$. The term s is the secretome signal-dependent $[R]$ production rate, calculated as $s(\sigma, t_n)$ at single cell level in Eq. S8. The d is the degradation constant for $[R]$ with unit s^{-1}. Solving for mean field steady state, we have $[R] = \frac{b+s}{d}$. The model parameters can be found in **Supplementary Table S2**.

Protrusion force induced by the regulator R

Considering all cells can form protrusions, with different protrusion forces, a minimal tumor migration model involves two main factors that contribute to the migration modes, the protrusion

force and cell-cell adhesion [4, 101]. Here, regulator R is capable to generate or regulate protrusion force. Possible force generating components may include cell cytoskeletons, such as F-actin and myosin [42], Rho signaling family proteins, such as Rac1 [28]. Thus, protrusion force $\vec{F}_\sigma$ for cell σ is described as follows, where f is the maximum protrusion force.

$$\vec{F}_\sigma = f\vec{p}_\sigma\left(\frac{[R]^4}{K_R^4 + [R]^4}\right) \tag{S10}$$

The impact of $[R]$ on cellular protrusion force is described as a Hill function, with half saturation concentration K_R. Higher $[R]$ can promote stronger protrusion for single cells. The $\vec{p}_\sigma$, the force polarity vector for cell σ, is determined by its own motion polarity $\vec{p}_{\sigma x}$ and neighboring cell polarity. Polarity is a directional vector for cell motion. Local polarity dissipation happens as friction exists between neighboring cells, where the direction of neighboring cell motion impacts the direction of motion of the cell σ. The force polarity $\vec{p}_\sigma$ is defined by the following expression:

$$\vec{p}_\sigma = \beta \sum_{i=1}^{n} \frac{\vec{p}_i}{n} + (1-\beta)\vec{p}_{\sigma x} \tag{S11}$$

$$\beta = \begin{cases} \beta_{max}\dfrac{\lambda_{fpp}}{\lambda_{fppb}} & if\ \dfrac{\lambda_{fpp}}{\lambda_{fppb}} < 1 \\ \beta_{max} & if\ \dfrac{\lambda_{fpp}}{\lambda_{fppb}} \geq 1 \end{cases} \tag{S12}$$

In Eq. S11, the $\vec{p}_\sigma$ is a linear combination of neighboring cell polarity and its own motion polarity, i is indexing the neighboring cell for cell σ, and n is the total number of neighboring cells for cell σ. In the first term of Eq. S11, β is the fraction of cellular polarity imposed by neighboring cells due to cell-cell interaction, with $\beta \in [0, \beta_{max}]$. β is determined by adhesion constraint λ_{fpp} in the model, as shown in Eq. S12. The second term $(1-\beta)$ in Eq. S11, is the fraction of cellular polarity from its own motion, i.e. cell σ's motion polarity, inferring that the cell's polarity persisted for a certain period. $\vec{p}_{\sigma x}$ is the cell polarity for past 5 MCS (Monte Carlo steps).

For Eq. S12, β_{max} is the maximum possible fraction of polarity that neighbors can impact a cell. λ_{fppb} is a constant for basal adhesion strength, and λ_{fpp} is the adhesion strength defined in Eq. S4. Eq. S12 describes the fact that stronger cell-cell adhesion allows neighboring cells to impose a stronger polarity alignment on cell σ .

Parameter scan for max protrusion force and adhesion strength

Two key parameters that determine tumor migration mode were scanned, including the maximum protrusion force (*f*) generated by a cell, and the strength of adhesion interactions between neighboring cells (λ_{fpp}). For each set of parameters, the simulation was run for 390 Monte Carlo steps (MCS), and repeated 50 times. The simulation included three steps. The first step was to relax the model to remove the dependence on the initial state set for the simulation. At the beginning of a simulation, the model was relaxed for 120 MCS. In the second step, we simulated the initial non-migratory tumor phenotype in the absence of any secretome signal. This step was run for 90 MCS with basal [R] production rate $b = 1\ \mu M/s$ and secretome signal-dependent $[R]$ production rate, $s = 0\ \mu M/s$ (no secretome, initially), mimicking the non-migratory 150 μm microtumor condition. In the third step, we simulated 150 μm microtumor treated with the hypoxic conditional media (secretome)setting the maximum secretome signal at tumor boundary to $s = 4\ \mu M/s$, with $b = 1\ \mu M/s$. The simulation was run for 180 MCS, corresponding to six days of experiment. Thus, each MCS corresponded to 48 min. For each simulation, we collected time lapse information, such as single cell positions, $[R]$ level, force $\vec{\mathrm{F}}_{\sigma}$, locally transmitted polarity fraction β, cell center of mass position. With the collected data, we obtained different migration modes. A phase graph can be found in **Figure S2**.

Total simulation time is a factor that may cause the migration landscape to change. For example, with a longer simulation time, the fraction of directional migration is expected to increase, as observed experimentally.

Identification of tumor migration modes

The migration modes of simulation results were determined with a two-step unsupervised clustering procedure using a set of nine geometric features of the microtumors. Figure S1 shows the distribution for all nine features. First, the migratory and non-migratory modes were identified with six distance-related measures, then the directionally and radially migratory tumors were classified with both the distance and the geometric shape features.

In step 1, in order to identify the migratory modes and non-migratory modes, we performed k-means clustering on the six distance-related features, including the displacement of the center of the tumor mass D_{tumor}, average cell displacement from initial tumor center $\bar{d}$, the standard deviation for cell displacement $D_{\sigma std}$, the average of radial distance measure to initial tumor center $D_{radialavg}$, the standard deviation of radial distance measure to initial tumor center $D_{radialstd}$, and the standard deviation of cell migration distance comparing to initial condition $D_{migrationstd}$. Definitions of the distance measures are given in **Supplementary Table S3**. Features were preprocessed before clustering to avoid bias and optimize clustering results. First, the distance features of the final time frame (270 MCS) were divided by initial condition values (except for the $D_{migrationstd}$), then normalized to a standard distribution with mean 0 and standard deviation 1. Then the normalized features were clustered with k-means clustering into two groups, corresponding to migratory and non-migratory tumors. **Figure S1c** gives the clustering result in the uniform manifold approximation (UMAP) space.

In step 2, to identify the radial and directional migratory tumors, we used a total of 19 geometric features, including 8 distance features and 11 shape features [102]. Figure S1a shows the distribution of the 19 geometric features of the simulated tumors. Again, we preprocessed the features before clustering. The features were first divided by their initial step values, and then normalized to a standard distribution with a mean of 0 and a standard deviation of 1. Next, we performed feature dimensional reduction with UMAP, followed by k-mean clustering on the

reduced features. For reproducibility, we used a fixed random seed for both UMAP and k-means. **Figure S1d** gives the clustering results in the UMAP space.

Supplementary Figures

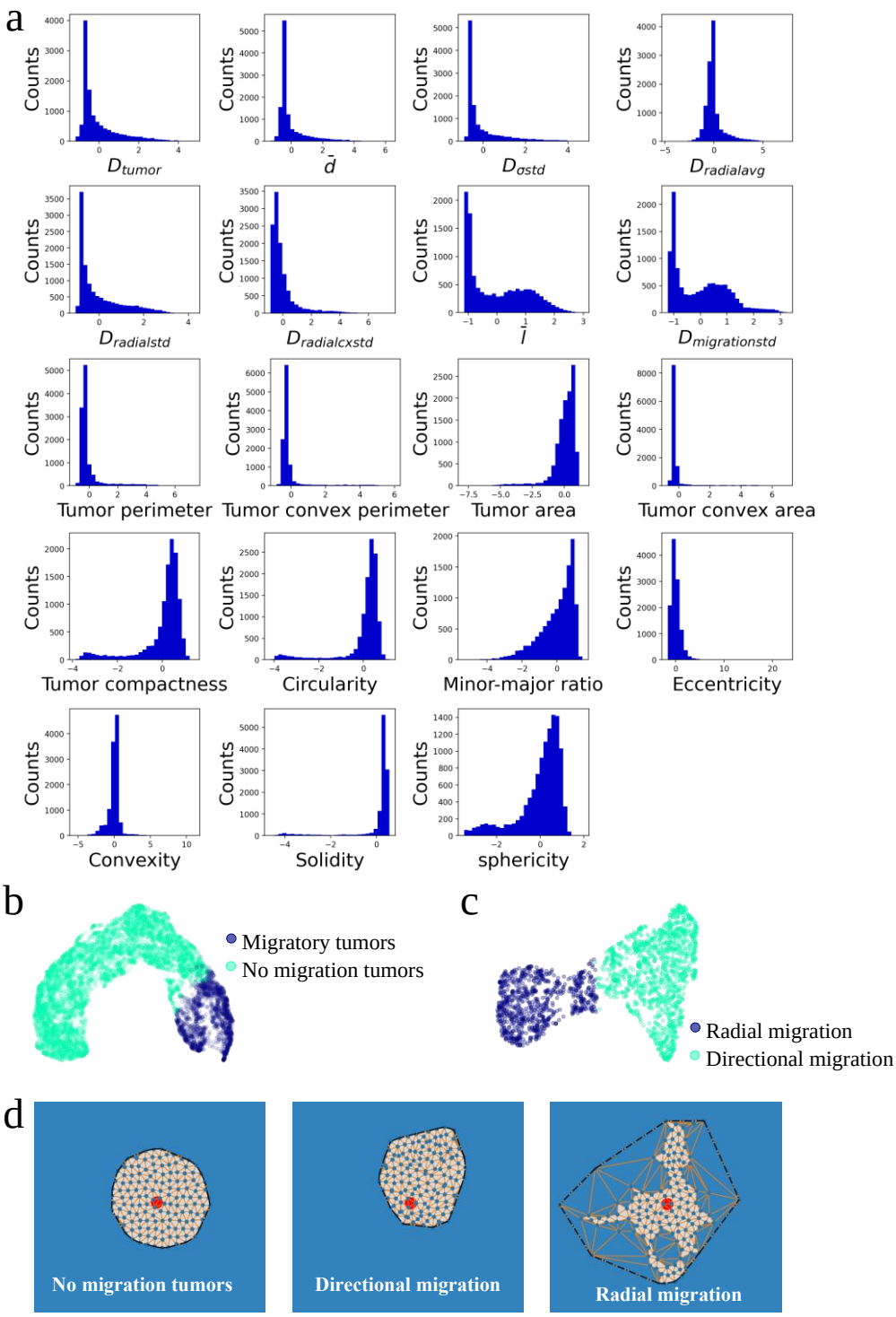

Figure S1. Tumor feature representations. **a.** Distribution of nineteen tumor features used for classification of tumor migration modes. **b.** UMAP representation for k-means clustering for distinguishing between non-migratory tumors and migratory tumors. **c.** UMAP representation for k-means clustering for distinguishing between radial migration and directional migration modes. **d.** Typical tumor morphologies at the final time frame for non-migratory, directionally migratory, and radially migratory tumors. Red dots are initial tumor centers. Blue dots are center coordinates for individual cells inside the tumors. Orange lines are calculated Delaunay triangles. Black dashed lines are convex hulls. The tumor area is filled with grey.

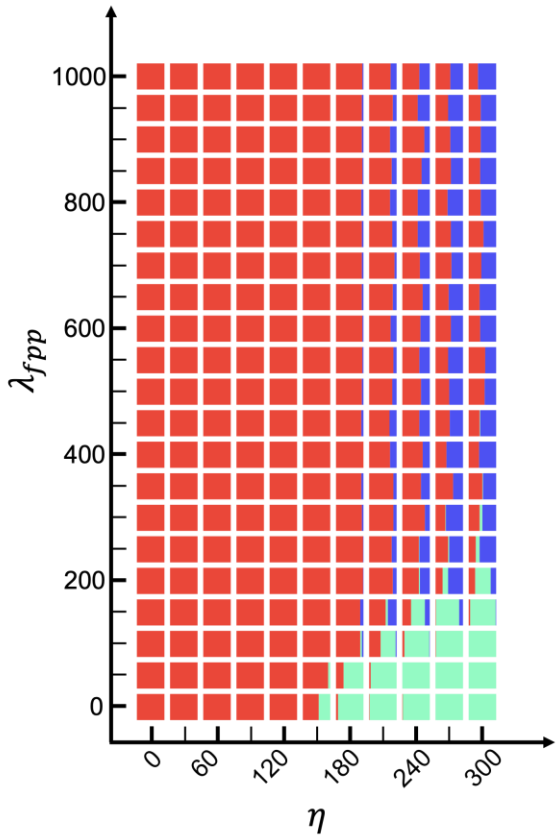

Figure S2. Phase graph showing tumor migration modes for parameter scan. On x axis, we scanned the maximum force η for range $[0,300]$. On y axis, we scanned the adhesion strength λ_{fpp} in range $[0,1000]$. The histogram is color-coded for non-migratory tumors (red), radially migrating tumors (green), and directionally migrating tumors (blue).

Supplementary Tables

Table S1. Multi-scale microtumor model parameters.

Parameter	Definition	Values
Dimensions	Lattice dimensions	256×256
T	Temperature	25
$J_{medium,medium}$	Bond energy (medium-medium)	-1
$J_{medium,cell}$	Bond energy (medium-cell)	-2
$J_{cell,cell}$	Bond energy (cell-cell)	-6
λ_{area}	Cell area constraint	4
A_{σ}	Cell target area	50.24
λ_{peri}	Cell perimeter constraint	4
L_{σ}	Cell target perimeter	25
λ_{fpp}	Focal point plasticity strength	[0, 1000]
$\mathrm{D}_{\sigma\omega}$	Spring length for focal point plasticity	8 pixel
s_{medium}	Constant secretome field in medium	1/pixel
D	Global secretome field diffusion constant	1
k_{uptake}	Cell (and protrusion cell) secretome relative uptake	0.0025/pixel
ζ	Coefficient for converting secretome uptake signal to production rate of R	Assigned during simulation
β_{max}	Neighbor sharing polarity constraint	0.4

Table S2. Parameter table of ODE dynamics for protrusion force.

Parameter	Definition	Values	Reference
b	Basal production rate protrusion force regulator, R	$1\ \mu M/s$	
s	Production rate of secretome-induced R. This parameter has the highest value at the tumor boundary.	$4\ \mu M/s$	
d	Degradation rate of protrusion force regulator, R	$0.1/s$	Estimated within reasonable range [103-106]
f	Maximum protrusion force	[0, 300]	
K_R	Half saturation concentration	$40\ \mu M$	Estimated within reasonable range [107]

Table S3. Geometric features were used for clustering the tumor migration modes.

#	Geometric features	Symbol	Formula	Annotation	Type
1	Displacement distance for the center of tumor mass	D_{tumor}	$D_{tumor} = \left\lvert \frac{\sum_{\sigma=1}^{N} \vec{x}_\sigma}{N} - \vec{\varepsilon} \right\rvert$	$\vec{x}_\sigma$ is the cell σ position vector at the final time frame (270 MCS*).	Distance measures
2	Average distance of displacement for cells	$\bar{d}$	$d_\sigma = \lvert \vec{x}_\sigma - \vec{\varepsilon} \rvert$ $D_{\sigma avg} = \frac{\sum_{\sigma=1}^{N} d_\sigma}{N}$	$\vec{x}_{\sigma init}$ is the cell σ position vector at the initial time frame (90 MCS).	
3	Standard deviation of d_σ	$D_{\sigma std}$	$D_{\sigma std} = \sqrt{\frac{\sum_{\sigma=1}^{N} (d_\sigma - \bar{d})^2}{N}}$	$\vec{\varepsilon}$ represent a vector for the initial tumor center, at pixel position $(128,128)$.	
4	Average radial distance measure	$D_{radialavg}$	$D_{radialavg} = \frac{\sum_{\sigma=1}^{M} d_\sigma}{M}$		
5	Standard deviation of radial distance measure	$D_{radialstd}$	$D_{radialstd} = \sqrt{\frac{\sum_{\sigma=1}^{M} (d_\sigma - \bar{d})^2}{M}})$	N is the number of cells in the tumor. M is the number of cells on the boundary of the tumor.	
6	Standard deviation of radial distance measure comparing to real time tumor center	$D_{radialcxstd}$	$r_\sigma = \vec{x}_\sigma - \frac{\sum_{\sigma=1}^{N} \vec{x}_\sigma}{N}$ $D_{radialcxstd} = \sqrt{\frac{\sum_{\sigma=1}^{M} (r_\sigma - \bar{r})^2}{M}}$	d_σ is the distance for cell σ position to the initial tumor center.	
7	Average cell migratory distance compared to	$\bar{l}$	$l_\sigma = \vec{x}_\sigma - \vec{x}_{\sigma init}$ $\bar{l} = \frac{\sum_{\sigma=1}^{N} l_\sigma}{N}$	l_σ is the distance for cell σ displacement	

	the initial state			compared to its initial position.	
8	Standard deviation of cell migratory distance compared to initial position.	$D_{migrations}$	$D_{migrationstd} = \sqrt{\frac{\sum_{\sigma=1}^{N}(l_\sigma - \bar{l})^2}{N}}$		
9	Tumor perimeter	P_{tumor}	The number of pixels on the edges of the tumor boundary, defined by Delaunay triangles.		Shape measures
10	Tumor convex perimeter	P_{convex}	The number of pixels on the edges of the convex hull.		
11	Tumor area	A_{tumor}	$A_{tumor} = \frac{\#\ of\ pixels\ in\ tumor}{256 \times 256}$	For simplicity, the tumor area is normalized by the simulation panel size	
12	Tumor convex area	A_{convex}	$A_{convex} = \frac{\#\ of\ pixels\ in\ convex\ hull}{256 \times 256}$	For simplicity, the tumor convex area is normalized by the simulation panel size	
13	Tumor compactness	$F_{compact}$	$F_{compact} = \frac{4\pi \cdot A_{tumor}}{P_{tumor}^2}$		
14	Tumor circularity	$F_{circularity}$	$F_{circular} = \frac{4\pi \cdot A_{tumor}}{P_{convex}^2}$	P_{convex} is the tumor perimeter calculated by the convex hull algorithm.	
15	Minor-major ratio	$F_{minormajor}$	$F_{minormajor} = \frac{D_{minor}}{D_{major}}$	D_{minor} is the length of the minor	

				axis of the ellipse that has the same normalized second central moments as the region. Similarly, D_{major} is the length for the major axis.	
16	Eccentricity	$F_{eccentricity}$	For an ellipse that has the same second moments as the tumor region, eccentricity is the ratio of the focal distance over the major axis length D_{major}.		
17	Convexity	$F_{convexity}$	$F_{convexity} = \frac{P_{convex}}{P_{tumor}}$		
18	Solidity	$F_{solidity}$	$F_{solidity} = \frac{A_{tumor}}{A_{convex}}$		
19	Sphericity	$F_{sphericity}$	$F_{sphericity} = \frac{R_{inscribing}}{R_{circumscribing}}$	$R_{inscribing}$ and $R_{circumscribing}$ are the radius of circles inscribing and circumscribing the tumor, respectively.	

Note: MCS*: Monte Carlo step

Reference

1. Eccles, S.A. and D.R. Welch, *Metastasis: recent discoveries and novel treatment strategies.* The Lancet, 2007. **369**(9574): p. 1742-1757.

2. Cheung, K.J. and A.J. Ewald, *A collective route to metastasis: Seeding by tumor cell clusters.* Science, 2016. **352**(6282): p. 167-9.

3. Woods, M.L., et al., *Directional collective cell migration emerges as a property of cell interactions.* PLoS One, 2014. **9**(9): p. e104969.

4. Friedl, P., Y. Hegerfeldt, and M. Tusch, *Collective cell migration in morphogenesis and cancer.* Int J Dev Biol, 2004. **48**(5-6): p. 441-9.

5. George, M., F. Bullo, and O. Campas, *Connecting individual to collective cell migration.* Sci Rep, 2017. **7**(1): p. 9720.

6. Friedl, P., et al., *Classifying collective cancer cell invasion.* Nat Cell Biol, 2012. **14**(8): p. 777-83.

7. Talmadge, J.E. and I.J. Fidler, *AACR centennial series: the biology of cancer metastasis: historical perspective.* Cancer Res, 2010. **70**(14): p. 5649-69.

8. Donato, C., et al., *Hypoxia Triggers the Intravasation of Clustered Circulating Tumor Cells.* Cell Rep, 2020. **32**(10): p. 108105.

9. Aceto, N., et al., *Circulating tumor cell clusters are oligoclonal precursors of breast cancer metastasis.* Cell, 2014. **158**(5): p. 1110-1122.

10. Filic, V., et al., *Regulation of the Actin Cytoskeleton via Rho GTPase Signalling in Dictyostelium and Mammalian Cells: A Parallel Slalom.* Cells, 2021. **10**(7).

11. Fukushima, S., S. Matsuoka, and M. Ueda, *Excitable dynamics of Ras triggers spontaneous symmetry breaking of PIP3 signaling in motile cells.* J Cell Sci, 2019. **132**(5).

12. Banerjee, T., et al., *A dynamic partitioning mechanism polarizes membrane protein distribution.* Nat Commun, 2023. **14**(1): p. 7909.

13. Xiong, Y., et al., *Cells navigate with a local-excitation, global-inhibition-biased excitable network.* Proc Natl Acad Sci U S A, 2010. **107**(40): p. 17079-86.

14. Ritch, S.J., et al., *Advanced assessment of migration and invasion of cancer cells in response to mifepristone therapy using double fluorescence cytochemical labeling.* BMC Cancer, 2019. **19**(1): p. 376.

15. Gau, D.M. and P. Roy, *Single Cell Migration Assay Using Human Breast Cancer MDA-MB-231 Cell Line.* Bio Protoc, 2020. **10**(8).

16. Valster, A., et al., *Cell migration and invasion assays.* Methods, 2005. **37**(2): p. 208-15.

17. Hira, V.V., et al., *2D and 3D in vitro assays to quantify the invasive behavior of glioblastoma stem cells in response to SDF-1α.* BioTechniques, 2020. **69**(5): p. 339-346.

18. Singh, M., et al., *Production of Uniform 3D Microtumors in Hydrogel Microwell Arrays for Measurement of Viability, Morphology, and Signaling Pathway Activation.* Assay Drug Dev Technol, 2015. **13**(9): p. 570-83.

19. Singh, M., et al., *Three-Dimensional Breast Cancer Models Mimic Hallmarks of Size-Induced Tumor Progression.* Cancer Res, 2016. **76**(13): p. 3732-43.

20. Singh, M., et al., *Controlled Three-Dimensional Tumor Microenvironments Recapitulate Phenotypic Features and Differential Drug Response in Early vs Advanced Stage Breast Cancer.* ACS Biomater Sci Eng, 2018. **4**(2): p. 421-431.

21. Singh, M., et al., *Targeting the Temporal Dynamics of Hypoxia-Induced Tumor-Secreted Factors Halts Tumor Migration.* Cancer Res, 2019. **79**(11): p. 2962-2977.

22. Dos Reis, R.S., et al., *Modeling HIV-1 neuropathogenesis using three-dimensional human brain organoids (hBORGs) with HIV-1 infected microglia.* Sci Rep, 2020. **10**(1): p. 15209.

23. Ardila, D.C., et al., *Identifying Molecular Signatures of Distinct Modes of Collective Migration in Response to the Microenvironment Using Three-Dimensional Breast Cancer Models.* Cancers, 2021. **13**(6): p. 1429.

24. Aggarwal, V., et al., *P4HA2: A link between tumor-intrinsic hypoxia, partial EMT and collective migration.* Adv Cancer Biol Metastasis, 2022. **5**: p. 100057.

25. Aggarwal, V., et al., *Interplay between tumor microenvironment and partial EMT as the driver of tumor progression.* iScience, 2021. **24**(2): p. 102113.

26. Fidler, I.J., *Critical determinants of metastasis.* Semin Cancer Biol, 2002. **12**(2): p. 89-96.

27. Mierke, C.T., *Mechanical Cues Affect Migration and Invasion of Cells From Three Different Directions.* Frontiers in Cell and Developmental Biology, 2020. **8**(946).

28. Fife, C.M., J.A. McCarroll, and M. Kavallaris, *Movers and shakers: cell cytoskeleton in cancer metastasis.* British journal of pharmacology, 2014. **171**(24): p. 5507-5523.

29. Small, J.V., et al., *The lamellipodium: where motility begins.* Trends Cell Biol, 2002. **12**(3): p. 112-20.

30. Pollard, T.D. and G.G. Borisy, *Cellular motility driven by assembly and disassembly of actin filaments.* Cell, 2003. **112**(4): p. 453-65.

31. Yilmaz, M., G. Christofori, and F. Lehembre, *Distinct mechanisms of tumor invasion and metastasis.* Trends in Molecular Medicine, 2007. **13**(12): p. 535-541.

32. Wilson, J.H.H.T., *Molecular biology of the cell, 4th edition : a problems approach*. 2002, New York; London: Garland Science.

33. Van Liedekerke, P., et al., *Simulating tissue mechanics with agent-based models: concepts, perspectives and some novel results.* Computational Particle Mechanics, 2015. **2**(4): p. 401-444.

34. Szabó, A. and R.M. Merks, *Cellular Potts Modeling of Tumor Growth, Tumor Invasion, and Tumor Evolution.* Frontiers in Oncology, 2013. **3**(87).

35. Graner, F. and J.A. Glazier, *Simulation of biological cell sorting using a two-dimensional extended Potts model.* Phys Rev Lett, 1992. **69**(13): p. 2013-2016.

36. Glazier, J.A. and F. Graner, *Simulation of the differential adhesion driven rearrangement of biological cells.* Phys Rev E Stat Phys Plasmas Fluids Relat Interdiscip Topics, 1993. **47**(3): p. 2128-2154.

37. Swat, M.H., et al., *Multi-scale modeling of tissues using CompuCell3D.* Methods Cell Biol, 2012. **110**: p. 325-66.

38. Mehidi, A., et al., *Transient Activations of Rac1 at the Lamellipodium Tip Trigger Membrane Protrusion.* Current Biology, 2019. **29**(17): p. 2852-2866.e5.

39. Sayyad, W.A., et al., *The role of myosin-II in force generation of DRG filopodia and lamellipodia.* Scientific Reports, 2015. **5**(1): p. 7842.

40. Yap, A.S., K. Duszyc, and V. Viasnoff, *Mechanosensing and Mechanotransduction at Cell-Cell Junctions.* Cold Spring Harb Perspect Biol, 2018. **10**(8).

41. Khataee, H., A. Czirok, and Z. Neufeld, *Multiscale modelling of motility wave propagation in cell migration.* Scientific Reports, 2020. **10**(1): p. 8128.

42. Svitkina, T., *The Actin Cytoskeleton and Actin-Based Motility.* Cold Spring Harb Perspect Biol, 2018. **10**(1).

43. Faix, J. and I. Weber, *A dual role model for active Rac1 in cell migration.* Small GTPases, 2013. **4**(2): p. 110-5.

44. de Beco, S., F. Amblard, and S. Coscoy, *Chapter two - New Insights into the Regulation of E-cadherin Distribution by Endocytosis*, in *International Review of Cell and Molecular Biology*, K.W. Jeon, Editor. 2012, Academic Press. p. 63-108.

45. Prahl, L.S. and D.J. Odde, *Modeling Cell Migration Mechanics*, in *Biomechanics in Oncology*, C. Dong, N. Zahir, and K. Konstantopoulos, Editors. 2018, Springer International Publishing: Cham. p. 159-187.

46. Friedl, P. and D. Gilmour, *Collective cell migration in morphogenesis, regeneration and cancer.* Nature Reviews Molecular Cell Biology, 2009. **10**(7): p. 445-457.

47. Shibata, K., et al., *Rac1 regulates myosin II phosphorylation through regulation of myosin light chain phosphatase.* J Cell Physiol, 2015. **230**(6): p. 1352-64.

48. Mishra, A.K., et al., *Coordination of protrusion dynamics within and between collectively migrating border cells by myosin II.* Mol Biol Cell, 2019. **30**(19): p. 2490-2502.

49. Hemmings, B.A. and D.F. Restuccia, *PI3K-PKB/Akt pathway.* Cold Spring Harb Perspect Biol, 2012. **4**(9): p. a011189.

50. Haggblad Sahlberg, S., et al., *Different functions of AKT1 and AKT2 in molecular pathways, cell migration and metabolism in colon cancer cells.* Int J Oncol, 2017. **50**(1): p. 5-14.

51. Linnerth-Petrik, N.M., et al., *Opposing functions of Akt isoforms in lung tumor initiation and progression.* PLoS One, 2014. **9**(4): p. e94595.

52. Riggio, M., et al., *AKT1 and AKT2 isoforms play distinct roles during breast cancer progression through the regulation of specific downstream proteins.* Sci Rep, 2017. **7**(1): p. 44244.

53. Zhou, G.L., et al., *Opposing roles for Akt1 and Akt2 in Rac/Pak signaling and cell migration.* J Biol Chem, 2006. **281**(47): p. 36443-53.

54. Polytarchou, C., et al., *Akt2 regulates all Akt isoforms and promotes resistance to hypoxia through induction of miR-21 upon oxygen deprivation.* Cancer Res, 2011. **71**(13): p. 4720-31.

55. Huttenlocher, A., R.R. Sandborg, and A.F. Horwitz, *Adhesion in cell migration.* Curr Opin Cell Biol, 1995. **7**(5): p. 697-706.

56. Mendonsa, A.M., T.Y. Na, and B.M. Gumbiner, *E-cadherin in contact inhibition and cancer.* Oncogene, 2018. **37**(35): p. 4769-4780.

57. Villagrasa, P., et al., *Akt2 interacts with Snail1 in the E-cadherin promoter.* Oncogene, 2012. **31**(36): p. 4022-4033.

58. Lan, A., Y. Qi, and J. Du, *Akt2 Mediates TGF-β1-Induced Epithelial to Mesenchymal Transition by Deactivating GSK3β/Snail Signaling Pathway in Renal Tubular Epithelial Cells.* Cellular Physiology and Biochemistry, 2014. **34**(2): p. 368-382.

59. Yang, Y., et al., *An emerging tumor invasion mechanism about the collective cell migration.* Am J Transl Res, 2019. **11**(9): p. 5301-5312.

60. Pantel, K. and R.H. Brakenhoff, *Dissecting the metastatic cascade.* Nature Reviews Cancer, 2004. **4**(6): p. 448-456.

61. Klameth, L., et al., *Small cell lung cancer: model of circulating tumor cell tumorospheres in chemoresistance.* Sci Rep, 2017. **7**(1): p. 5337.

62. Yu, N., et al., *Circulating tumor cells in lung cancer: detection methods and clinical applications.* Lung, 2015. **193**(2): p. 157-71.

63. Schuster, E., et al., *Better together: circulating tumor cell clustering in metastatic cancer.* Trends Cancer, 2021. **7**(11): p. 1020-1032.

64. Yamamoto, A., A.E. Doak, and K.J. Cheung, *Orchestration of Collective Migration and Metastasis by Tumor Cell Clusters.* Annu Rev Pathol, 2023. **18**: p. 231-256.

65. Alexandrova, A. and M. Lomakina, *How does plasticity of migration help tumor cells to avoid treatment: Cytoskeletal regulators and potential markers.* Front Pharmacol, 2022. **13**: p. 962652.

66. Nagai, T., et al., *Tactics of cancer invasion: solitary and collective invasion.* J Biochem, 2020. **167**(4): p. 347-355.

67. Wu, J.S., et al., *Plasticity of cancer cell invasion: Patterns and mechanisms.* Transl Oncol, 2021. **14**(1): p. 100899.

68. Hapach, L.A., et al., *Phenotypic Heterogeneity and Metastasis of Breast Cancer Cells.* Cancer Res, 2021. **81**(13): p. 3649-3663.

69. Limia, C.M., et al., *Emerging Roles of the Endoplasmic Reticulum Associated Unfolded Protein Response in Cancer Cell Migration and Invasion.* Cancers (Basel), 2019. **11**(5).

70. Song, D., et al., *Pathway-based analysis of breast cancer.* Am J Transl Res, 2014. **6**(3): p. 302-11.

71. Yousefnia, S., et al., *Mechanistic Pathways of Malignancy in Breast Cancer Stem Cells.* Frontiers in Oncology, 2020. **10**.

72. Kai, F., H. Laklai, and V.M. Weaver, *Force Matters: Biomechanical Regulation of Cell Invasion and Migration in Disease.* Trends in Cell Biology, 2016. **26**(7): p. 486-497.

73. Koch, T.M., et al., *3D Traction forces in cancer cell invasion.* PloS one, 2012. **7**(3): p. e33476-e33476.

74. Janiszewska, M., M.C. Primi, and T. Izard, *Cell adhesion in cancer: Beyond the migration of single cells.* The Journal of biological chemistry, 2020. **295**(8): p. 2495-2505.

75. Collins, C. and W.J. Nelson, *Running with neighbors: coordinating cell migration and cell-cell adhesion.* Curr Opin Cell Biol, 2015. **36**: p. 62-70.

76. Cowan, J.M., et al., *Non-muscle myosin II and the plasticity of 3D cell migration.* Frontiers in Cell and Developmental Biology, 2022. **10**.

77. Kovacs, M., et al., *Mechanism of blebbistatin inhibition of myosin II.* J Biol Chem, 2004. **279**(34): p. 35557-63.

78. Li, Y.R. and W.X. Yang, *Myosins as fundamental components during tumorigenesis: diverse and indispensable.* Oncotarget, 2016. **7**(29): p. 46785-46812.

79. Tse, J.M., et al., *Mechanical compression drives cancer cells toward invasive phenotype.* Proceedings of the National Academy of Sciences, 2012. **109**(3): p. 911-916.

80. Grieve, A.G. and C. Rabouille, *Extracellular cleavage of E-cadherin promotes epithelial cell extrusion.* J Cell Sci, 2014. **127**(Pt 15): p. 3331-46.

81. Chang, P.-H., et al., *Interplay between desmoglein2 and hypoxia controls metastasis in breast cancer.* Proceedings of the National Academy of Sciences, 2021. **118**(3): p. e2014408118.

82. Wrenn, E.D., et al., *Regulation of Collective Metastasis by Nanolumenal Signaling.* Cell, 2020. **183**(2): p. 395-410 e19.

83. Higginbotham, J.N., et al., *Amphiregulin exosomes increase cancer cell invasion.* Curr Biol, 2011. **21**(9): p. 779-86.

84. Roh-Johnson, M., et al., *Macrophage-Dependent Cytoplasmic Transfer during Melanoma Invasion In Vivo.* Dev Cell, 2017. **43**(5): p. 549-562 e6.

85. Li, Z., et al., *Hotspot ESR1 Mutations Are Multimodal and Contextual Modulators of Breast Cancer Metastasis.* Cancer Res, 2022. **82**(7): p. 1321-1339.

86. Friedl, P. and R. Mayor, *Tuning Collective Cell Migration by Cell-Cell Junction Regulation.* Cold Spring Harb Perspect Biol, 2017. **9**(4).

87. Na, T.-Y., et al., *The functional activity of E-cadherin controls tumor cell metastasis at multiple steps.* Proceedings of the National Academy of Sciences, 2020. **117**(11): p. 5931-5937.

88. Balamurugan, K., et al., *Stabilization of E-cadherin adhesions by COX-2/GSK3β signaling is a targetable pathway in metastatic breast cancer.* JCI Insight, 2023. **8**(6).

89. Shen, M. and Y. Kang, *Role Reversal: A Pro-metastatic Function of E-Cadherin.* Dev Cell, 2019. **51**(4): p. 417-419.

90. Fearon, E.R., *Cancer: Context Is Key for E-cadherin in Invasion and Metastasis.* Current Biology, 2019. **29**(21): p. R1140-R1142.

91. Padmanaban, V., et al., *E-cadherin is required for metastasis in multiple models of breast cancer.* Nature, 2019. **573**(7774): p. 439-444.

92. Gradeci, D., et al., *Cell-scale biophysical determinants of cell competition in epithelia.* eLife, 2021. **10**: p. e61011.

93. Indana, D. and O. Chaudhuri, *Cells under pressure*. eLife, 2021. **10**: p. e68643.

94. Djagaeva, I. and S. Doronkin, *Hypoxia response pathway in border cell migration.* Cell adhesion & migration, 2010. **4**(3): p. 391-395.

95. Allingham, J.S., R. Smith, and I. Rayment, *The structural basis of blebbistatin inhibition and specificity for myosin II.* Nat Struct Mol Biol, 2005. **12**(4): p. 378-9.

96. Yap, T.A., et al., *Preclinical pharmacology, antitumor activity, and development of pharmacodynamic markers for the novel, potent AKT inhibitor CCT128930.* Mol Cancer Ther, 2011. **10**(2): p. 360-71.

97. Nitulescu, G.M., et al., *Akt inhibitors in cancer treatment: The long journey from drug discovery to clinical use (Review).* Int J Oncol, 2016. **48**(3): p. 869-85.

98. Meng, W. and M. Takeichi, *Adherens junction: molecular architecture and regulation.* Cold Spring Harb Perspect Biol, 2009. **1**(6): p. a002899.

99. Pally, D., D. Pramanik, and R. Bhat, *An Interplay Between Reaction-Diffusion and Cell-Matrix Adhesion Regulates Multiscale Invasion in Early Breast Carcinomatosis.* Frontiers in Physiology, 2019. **10**(790).

100. Yamaguchi, H. and J. Condeelis, *Regulation of the actin cytoskeleton in cancer cell migration and invasion.* Biochim Biophys Acta, 2007. **1773**(5): p. 642-52.

101. Schwartz, M.A. and A.R. Horwitz, *Integrating Adhesion, Protrusion, and Contraction during Cell Migration.* Cell, 2006. **125**(7): p. 1223-1225.

102. Wang, W., et al., *Live-cell imaging and analysis reveal cell phenotypic transition dynamics inherently missing in snapshot data.* Sci Adv, 2020. **6**(36).

103. Zhang, B. and Y. Zheng, *Regulation of RhoA GTP hydrolysis by the GTPase-activating proteins p190, p50RhoGAP, Bcr, and 3BP-1.* Biochemistry, 1998. **37**(15): p. 5249-57.

104. Bolado-Carrancio, A., et al., *Periodic propagating waves coordinate RhoGTPase network dynamics at the leading and trailing edges during cell migration.* eLife, 2020. **9**: p. e58165.

105. Mori, Y., A. Jilkine, and L. Edelstein-Keshet, *Wave-Pinning and Cell Polarity from a Bistable Reaction-Diffusion System.* Biophysical Journal, 2008. **94**(9): p. 3684-3697.

106. Byrne, K.M., et al., *Bistability in the Rac1, PAK, and RhoA Signaling Network Drives Actin Cytoskeleton Dynamics and Cell Motility Switches.* Cell Syst, 2016. **2**(1): p. 38-48.

107. Huang, B., et al., *The three-way switch operation of Rac1/RhoA GTPase-based circuit controlling amoeboid-hybrid-mesenchymal transition.* Scientific Reports, 2014. **4**(1): p. 6449.